Research in Astronomy and Astrophysics, 22:072003 (28pp), 2022 July https://doi.org/10.1088/1674-4527/ac77e4

CHES: A Space-borne Astrometric Mission for the Detection of Habitable Planets of the Nearby Solar-type Stars

Jiang-Hui Ji[1,2], Hai-Tao Li[3,4], Jun-Bo Zhang[5,6], Liang Fang[4,5,7], Dong Li[8], Su Wang[1,2], Yang Cao[3], Lei Deng[8], Bao-Quan Li[3,4], Hao Xian[4,5,6], Xiao-Dong Gao[5], Ang Zhang[4,5,6], Fei Li[8], Jia-Cheng Liu[9], Zhao-Xiang Qi[10], Sheng Jin[1,2], Ya-Ning Liu[3], Guo Chen[1,2], Ming-Tao Li[3,4], Yao Dong[1,2], and Zi Zhu[9]

CHES consortium

[1] CAS Key Laboratory of Planetary Sciences, Purple Mountain Observatory, Chinese Academy of Sciences, Nanjing 210023, China; jijh@pmo.ac.cn
[2] School of Astronomy and Space Science, University of Science and Technology of China, Hefei 230026, China
[3] Key Laboratory of Electronics and Information Technology for Space Systems, National Space Science Center, Chinese Academy of Sciences, Beijing 100190, China
[4] University of Chinese Academy of Sciences, Beijing 100049, China
[5] Institute of Optics and Electronics, Chinese Academy of Sciences, Chengdu 610209, China
[6] Key Laboratory on Adaptive Optics, Chinese Academy of Sciences, Chengdu 610209, China
[7] Key Laboratory of Science and Technology on Space Optoelectronic Precision Measurement, Chinese Academy of Sciences, Chengdu 610209, China
[8] Innovation Academy for Microsatellites of Chinese Academy of Sciences, Shanghai 201306, China
[9] School of Astronomy and Space Science, Nanjing University, Nanjing 210046, China
[10] Shanghai Astronomical Observatory, Chinese Academy of Sciences, Shanghai 200030, China
Received 2022 April 29; revised 2022 June 4; accepted 2022 June 9; published 2022 July 8

Abstract

The Closeby Habitable Exoplanet Survey (CHES) mission is proposed to discover habitable-zone Earth-like planets of nearby solar-type stars (~10 pc away from our solar system) via microarcsecond relative astrometry. The major scientific objectives of CHES are: to search for Earth Twins or terrestrial planets in habitable zones orbiting 100 FGK nearby stars; further to conduct a comprehensive survey and extensively characterize nearby planetary systems. The primary payload is a high-quality, low-distortion, high-stability telescope. The optical subsystem is a coaxial three-mirror anastigmat (TMA) with a 1.2 m-aperture, $0\overset{\circ}{.}44 \times 0\overset{\circ}{.}44$ field of view and 500 nm−900 nm working wave band. The camera focal plane is composed of a mosaic of 81 scientific CMOS detectors each with 4 k × 4 k pixels. The heterodyne laser interferometric calibration technology is employed to ensure microarcsecond level (1 μas) relative astrometry precision to meet the requirements for detection of Earth-like planets. The CHES satellite operates at the Sun–Earth L2 point and observes all the target stars for 5 yr. CHES will offer the first direct measurements of true masses and inclinations of Earth Twins and super-Earths orbiting our neighbor stars based on microarcsecond astrometry from space. This will definitely enhance our understanding of the formation of diverse nearby planetary systems and the emergence of other worlds for solar-type stars, and finally provide insights to the evolution of our own solar system.

Key words: Astrometry and Celestial Mechanics – planets and satellites: detection – planets and satellites: terrestrial planets – stars: solar-type

1. Executive Summary

1.1. CHES's Major Scientific Goals

Discovering and exploring habitable planets in our Galaxy will provide essential answers to *"Are we alone in the universe?", "Is the Earth unique?", "How planets evolve to the cradle of life?"* or *"Is our solar system special?"*. The in-depth understanding of the formation and evolution of planetary systems necessarily relies on the detection of diverse exoplanets (especially habitable planets), which is of great significance to enriching human beings' exploration of unknown worlds, shedding light on the origin and evolution of life, and recognizing our status in the universe.

The Closeby Habitable Exoplanet Survey (CHES) mission is proposed to discover Earth-like planets around nearby solar-type stars via ultra-high-precision relative astrometry. The key scientific goals are:

(1) to search for terrestrial planets in habitable zones orbiting 100 FGK stars ~10 pc from Earth (the nearby solar-type stars);

(2) further to conduct a comprehensive survey and extensive characterization of nearby planetary systems.

CHES will offer the first direct measurements of true masses and inclinations of *Earth Twins* (with orbit, mass and environment similar to Earth) and super-Earths orbiting our neighbor stars based on microarcsecond astrometry from space. This will definitely enhance our understanding of the formation

of diverse nearby planetary systems and the emergence of other worlds in nearby solar-type stars, and finally to investigate the origin and evolution of our own solar system.

1.2. Scientific Instruments

The payload is a high-quality, low-distortion, high-stability telescope with an optical subsystem, camera subsystem and on-board calibration subsystem. The optical subsystem is a coaxial three-mirror anastigmat (TMA) with a 1.2 m-aperture, $0.^{\circ}44 \times 0.^{\circ}44$ field of view (FOV) and 500 nm − 900 nm working wave band. The camera focal plane is composed of a mosaic of 81 scientific CMOS detectors, each with 4 k × 4 k pixels. The on-board calibration subsystem consists of a metrology assembly. A heterodyne laser interferometric calibration technology is employed to ensure microarcsecond level (1 μas) relative astrometry precision that is required to detect the habitable *Earth Twins* orbiting our neighboring stars.

The mission orbit of the CHES satellite will be about the L2 point of the Sun and the Earth. The satellite is designed to have a lifespan of 5 yr, during which all target stars will be extensively stared at and observed.

1.3. Additional Scientific Benefits

CHES will produce fruitful achievements not only in the aspect of Earth-like planets but also for cosmology, dark matter and black holes with microarcsecond accuracy in relative astrometry, which will better help us understand philosophy, life and planetary science.

Science case	Habitable Exoplanets orbiting nearby solar-type stars
Science objectives	> To discover habitable Earths around nearby solar-type stars. > To conduct a comprehensive survey and census on nearby planetary systems *Extended: cosmology, dark matter and black holes.*
Overview	> Spacecraft at L2 for 5 yr. > Optical telescope (500 nm−900 nm). > Microarcsecond astrometry (1 μas). > Point and stare strategy to enable relative astrometry.
What makes CHES unique?	> Ultra-high-precision relative astrometry simply reachable from space: 0.3 μas (habitable-zone Earths around Sun-like stars at 10 pc). > To obtain true masses and orbital architecture (inclinations, etc.) of habitable-zone terrestrial planets. > To conduct a census and characterization of nearby planetary systems.
Primary targets	> Nearby F, G, K stellar systems (100 stars ∼10 pc). *Extended: ultra-faint dwarf galaxies, neutron stars in X-ray binaries, etc.*
Scientific payload	> Coaxial three-reflection TMA system. > Primary mirror: $D = 1.2$ m diameter > Long focal length: $f = 36$ m. > FOV: $0.^{\circ}44 \times 0.^{\circ}44$, with six to eight reference stars. > Focal plane with 81 scientific CMOS detectors (4 k × 4 k, ⩾50 fps). > Nyquist sampling of the PSF. > Metrology calibration of the FPA: relative positions of pixels at the micropixel level for each detector, geometrical parameters of FPA.
Spacecraft	> Spacecraft dry mass with margin: 1,558 kg. Launch Mass: 2,930 kg, fuel mass (990 kg + 382 kg). > Attitude Control System: pointing accuracy of $0.''07$, pointing stability of $0.''0036/0.02$ s > Propulsion system: orbital maneuvering engines: 490 N + 12 × 10 N, attitude control thrusters: 12 × (1μN ∼ 50μ N) + 12 × 20 mN. > Thermal Control System: working temperature: 20 ± 5° C and temperature stability of 45 mK for payload; working temperature: −15 ∼ +45° C for other equipment. > Telecommand: X-band, communication rate: 20 Mbps.
Launcher and operations	> CZ-3C: GTO (200 km × 35,958 km). > Orbital maneuver to halo orbit at L2. > Launch in 2025. > Nominal mission: 5 yr. > Launch site: Xichang.

2. Scientific Goals

As of today, more than 5000 exoplanets have been detected (https://exoplanetarchive.ipac.caltech.edu) since the first planet around the main-sequence star 51 Peg was discovered (Mayor & Queloz 1995). The statistical investigations on a large sample of exoplanets show that the planetary systems are actually complex and diverse far beyond our imagination. Figure 1 displays the planetary mass versus orbital period of exoplanets (Borucki et al. 2010, 2011; Batalha et al. 2013; Huang et al. 2018). Unlike their siblings in the solar system (marked by the filled squares with capital letters), these planets can be classified into hot Jupiters, cold Jupiters, warm Neptunes, super-Earths and terrestrial planets, where the color of the legends represents their surface temperature. However, real Earth-mass planets in the habitable-zone remain undetected. Therefore, the discovery of habitable-zone planets of solar-type stars and the characterization of rocky planets have become one of the most significant frontiers in the study of exoplanets.

Exploring Earth-like planets in the habitable zone (i.e., an Earth Twin or ET 2.0) will definitely provide clues to the

essential scientific questions such as *"Are we alone in the universe"* or *"How planets become the cradle of life?"*. The primary scientific goals of CHES will be to discover and explore terrestrial planets in the habitable zones orbiting nearby solar-type stars, and further conduct characterization of rocky planets, using ultra-high-precision relative astrometry.

2.1. Science Objective 1: Search for Terrestrial Planets in the Habitable Zone

To search for terrestrial planets in the habitable zone orbiting 100 FGK stars in the solar system's nearest neighbors (∼10 pc), and discover terrestrial planets in the habitable zone of nearby stars.

As is well-known, a number of space-borne missions for the detection of exoplanets have been carried out since 2000, e.g., the Global Astrometric Interferometer for Astrophysics (Gaia) satellite (Lindegren & Perryman 1996; Clementini et al. 2016) utilizing the astrometric method, the Kepler space telescope (Koch et al. 1998; Borucki et al. 2010), Transiting Exoplanet Survey Satellite (TESS) (Ricker et al. 2015), the CHaracterising ExOPlanet Satellite (CHEOPS) (Broeg et al. 2013), etc. employing the transit method. The Kepler mission contributed more than half of the discovered exoplanets (Borucki et al. 2011; Batalha et al. 2013), which give new insights into the orbital architecture, formation and dynamical evolution of planetary systems.

Future missions aiming at exoplanets include the Chinese Space Station Telescope (CSST) equipped with a coronagraph using direct imaging (Gao et al. 2015), the Nancy Grace Roman Space Telescope (Green et al. 2012) with microlensing, the PLAnetary Transits and Oscillations of stars (PLATO) (Ragazzoni et al. 2016), Atmospheric Remote-sensing Infrared mission Exoplanet Large-survey (ARIEL) (Tinetti et al. 2016), etc. Undoubtedly, these missions will considerably enable us to have an in-depth understanding of exoplanets, however as Figure 2 demonstrates, the habitable-zones for Earth-like planets orbiting nearby solar-type stars are rarely found, where the Earth is indicated by a red dot whereas blue circles stand for warm terrestrial planets and super-Earths, and the three separated curves, respectively from left to right, indicate the habitable border of a Recent Venus, Runaway Greenhouse and Early Mars (Kopparapu et al. 2013).

CHES will specifically target the terrestrial planets in habitable zones using the ultra-high-precision relative astrometric method in comparison with transit detection such as Kepler, TESS, CHEOPS, ARIEL, PLATO and several astrometric space mission concepts such as SIM (Catanzarite et al. 2005), NEAT (Malbet et al. 2012), STEP (Chen 2014), Theia (The Theia Collaboration et al 2017) and MASS (Nemati et al. 2020). CHES will be the first mission to directly focus on Earth-mass planets in the habitable zone about nearby solar-type stars. The scientific questions to be solved include whether there are planets in the habitable zone

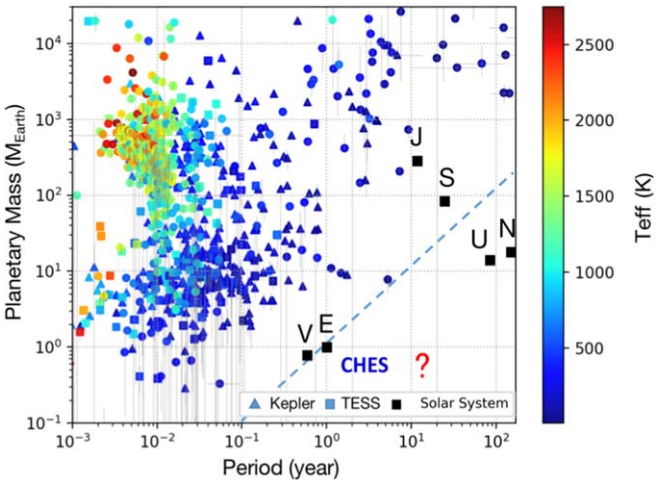

Figure 1. Mass and orbital period distribution of exoplanets.

orbiting nearby stars to our solar system, how these planets are distributed and what is the probability of occurrence for habitable-zone planets. Therefore, searching for habitable-zone planets in the solar system's neighbors by CHES can offer a significant clue to the distribution of nearby solar-type stars, especially those terrestrial planets in the habitable zone.

2.1.1. Terrestrial Planets in the Habitable Zone

As of March 2022, there are 38 terrestrial planets in the habitable zone discovered, most of which are around M-type stars (Gillon et al. 2017; Luger et al. 2017; Günther et al. 2019), mainly detected through transit photometry and radial velocity (RV). However, the transit method can only measure the size of a planet rather than its true mass, and the RV measurement can simply unveil the minimum mass of the planets (all of which are much larger than Earth), so it is not yet possible to confirm whether these planets are habitable-zone terrestrial planets.

The planetary candidates in the habitable zone discovered by Kepler are generally far away (1000–3000 light years) (Borucki et al. 2013), which makes them difficult to verify and further identify through other observational means. Most of the habitable-zone planets observed are moving around M dwarf stars with close-in orbits (Luger et al. 2017; Tsiaras et al. 2019), which may have strong ultraviolet radiation, and the atmospheric stability of the surrounding planets is uncertain. Therefore, whether these terrestrial planets in the habitable zone are habitable still remains controversial. Finally, some terrestrial planets in the habitable zone lack key information such as mass and size due to the limitation of observation, so it is still controversial whether they are terrestrial planets. Therefore,

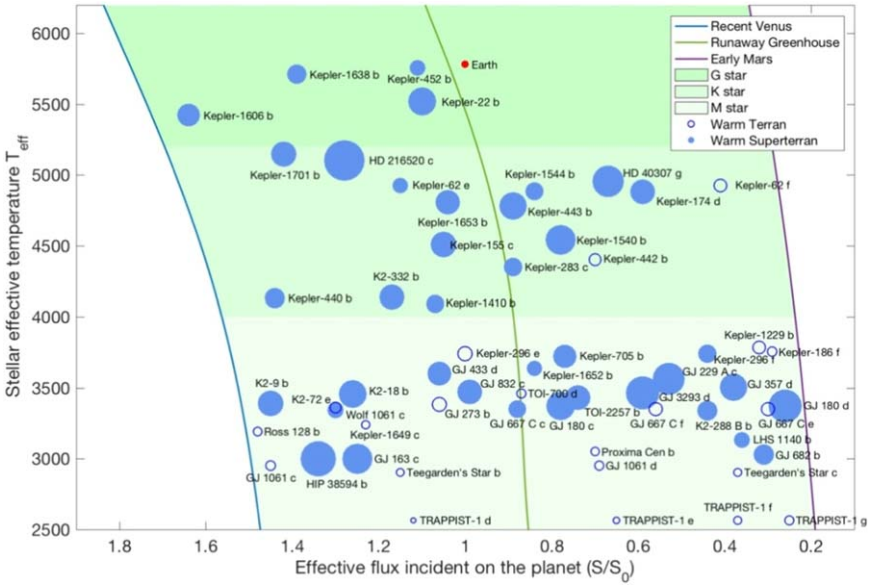

Figure 2. Distribution of known habitable-zone planets.

generally speaking, so far, real *Earth Twins* have not been found yet.

2.1.2. Detection of Terrestrial Planets Around Nearby Stars

The detection of habitable planets requires high precision (astrometry requires a microarcsecond level), and ground-based detection equipment is hard to break through the limit of 0.1 milliarcsecond accuracy due to atmospheric disturbance and other factors, even if it adopts technologies such as active optics. Therefore, space telescopes have turned out to be ideal for high-precision astronomical observations in addition to terrestrial spectroscopy (suitable for detecting planets with very short periods). However, it is rather difficult to detect habitable planets around Sun-like stars using the RV due to the influence of stellar activities, which cannot attain the true mass of the planet; a transit requires that the orbital plane of the planet aligns with the line of sight of the observers, which leads to a tiny probability of detection; direct imaging is inclined to find planets with larger masses and distant orbits from the host stars based on the present best accuracy of observation; microlensing can only obtain information about individual planets that are relatively far away and cannot be applicable to detecting nearby planets. As compared to the above-mentioned methods, the exoplanet detection of astrometry will have unbiased observations. Figure 3 shows the detection capability of terrestrial planets for the CHES mission in comparison with Kepler and high-precision RV (see also Zhu & Dong 2021), indicating that the astrometry of CHES will be advantageous in discovering habitable-zone Earth-like planets revolving around nearby stars.

In the next decade or two, habitable planets proximate to our solar system are the only places where traces of other forms of life can be found by observing the composition of the atmosphere (e.g., Des Marais et al. 2002; Kaltenegger 2017), and as well it is first necessary to detect such terrestrial planets in the habitable zone to explore the atmospheric composition of habitable planets. If many of these "Proxima-type planets" (Anglada-Escudé et al. 2016) are observed in the future, we can preferentially select observed objects like Earth-mass planets among these candidates. Therefore, identifying terrestrial planets in the habitable zone of nearby stars will greatly contribute to the primary goal of investigating extraterrestrial life.

2.1.3. Planetary Habitability

Planetary atmospheres are critical for characterizing planetary features, which may provide potential clues to the history of planetary formation and evolution, and are the basis for assessing planetary habitability (Kaltenegger 2017; Madhusudhan 2019; Zhang 2020). At present, the observation and characterization of exoplanet atmospheres mainly focus on gaseous planets, most of which are indirectly observed by transit or Doppler spectroscopy, and a small number of hot gas-giants in distant orbits can be directly imaged. The observation limit of indirect detection is expected to be extended to rocky planets, even including a small number of terrestrial planets located in the habitable zone of M dwarf stars after James Webb Space Telescope (JWST), ARIEL

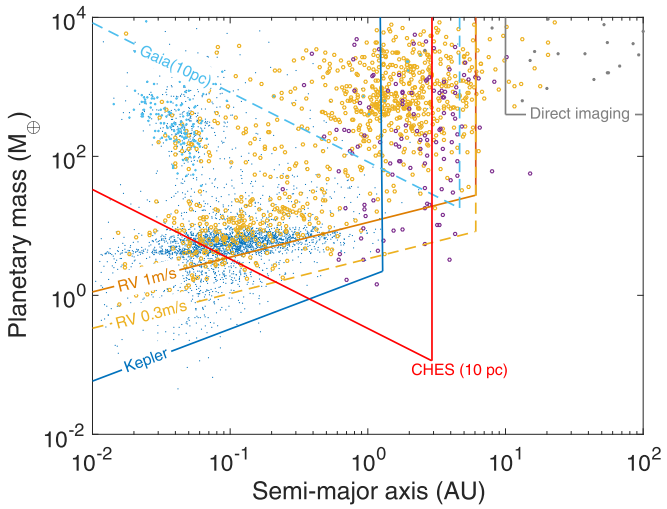

Figure 3. The detection capability of terrestrial planets for the CHES mission.

and other missions are performed. However, the luminosity and spectral line profile changes caused by the stellar activity make it extremely challenging to use indirect means to characterize the atmospheres of terrestrial planets in the habitable zone of solar-type stars. The effects of stellar activity can only be bypassed by direct imaging of planetary signals.

The next-generation flagship ground-based Very Large Aperture Telescope or Space Large Aperture Telescope will change this situation and make the atmospheric characterization of planets in the habitable zone of nearby stars feasible, thereby providing important observational evidence for assessing the habitability of potential Earth twins. According to the previous simulations (Snellen et al. 2015; Wang et al. 2017; Hawker & Parry 2019), large aperture ground-based telescopes aided by extreme adaptive optics, equipped with a high suppression ratio coronagraph and high dispersion spectrometer, will be able to directly obtain the reflection spectrum and thermal emission spectrum of the atmospheres of terrestrial planets in the habitable zone of nearby stars, and search for the presence of oxygen, water, methane, carbon dioxide and other components. METIS for the European Extremely Large Telescope (E-ELT) (Brandl et al. 2012), and PCS (Kasper et al. 2021) and PSI for the Thirty Meter Telescope (TMT) (Fitzgerald et al. 2019) are expected to make such observations a reality. On the other hand, space-borne telescopes with no influence from the Earth's atmosphere, equipped with both high suppression ratio coronagraphs and star shadows, such as HabEx (Gaudi et al. 2020) or LUVOIR (The LUVOIR Team 2019), would be more effective and direct for characterizing the atmospheres of terrestrial planets in the habitable zone of nearby stars, by measuring the chemical abundances of various biomarker molecules, so that the habitability of the related planets can be obtained, and even the existence of signs of biological activities can be assessed (Krissansen-Totton et al. 2018).

2.2. Science objective 2: A Comprehensive Census of Nearby Planetary Systems

Detecting planets with orbital periods of 30 days to 10 yr around *F*, *G*, *K* stars ∼10 pc from the solar system, and planets whose masses are greater than that of the Earth, provides the planet's true mass and three-dimensional orbital parameters, and establishes a complete exoplanet archive on nearby planetary systems.

2.2.1. Completeness Census of Nearby Planets

A more comprehensive exploration of the completeness of exoplanetary systems may cast light on the scenario of planetary formation and orbital evolution characteristics. Currently, various methods have a selective effect on planetary detection, especially RV and transit methods, which are usually simply suitable for the discovery of low-mass planets with orbital periods less than tens of days (Figure 4) (Berger et al. 2018), and planetary masses that cannot be decoupled or depend on special orbital configurations. However, CHES can directly give accurate planetary masses and orbital periods of planets, so it will carry out a more comprehensive and accurate study on planetary systems of nearby stars, which will play an important role in the completeness of planetary systems. Furthermore, CHES will be helpful to comprehensively and systematically understand the orbital characteristics, formation and evolution of planetary systems, and finally infer whether our solar system is universal or unique.

The planetary formation theory suggests that planetary systems around stars are ubiquitous, and the mass distribution of planets in the system is similar to the distribution of planets in our own solar system; but most of the planets discovered so far are much larger than the mass of the Earth, mainly owing to the selection effect induced by the limitations of observational methods: the transit detection is inclined to detect large-size planets with short-period orbits in the line of sight of the observer, while the RV method is prone to find massive planets with close-in orbits. The data released by Kepler (Figure 4) show that the distribution of planetary radii affirms that there is a deep distribution gap between 1.5 and 2.0 Earth radii, and regions with a planetary radius less than 1.14 Earth radii are less complete. This feature may also imply some undiscovered regularity (Fulton et al. 2017; Berger et al. 2018), which may result from the photoevaporation model (Owen & Wu 2017). In addition to the discovery of habitable planets, the ultra-high-precision detection capabilities of CHES will also be able to conduct relatively comprehensive detection and investigation on nearby planetary systems, to discover the planets from ET 2.0 to super-Earth in the habitable zones, thereby helping reveal the formation and evolution mechanisms of a wide variety of planets.

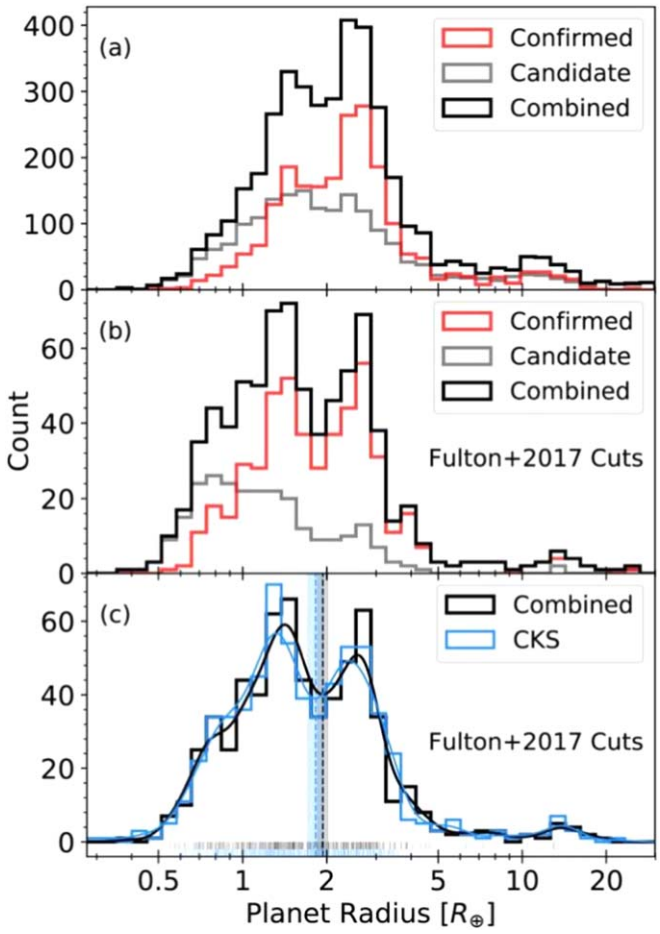

Figure 4. Planetary radius distribution of Kepler's released candidates (Berger et al. 2018).

2.2.2. The True Mass of a Planet

In addition to its orbital characteristics, the internal structure of the planet also plays a key part in determining its physical properties and evaluates whether it is habitable. According to current theory, a habitable planet must first have a solid or liquid surface; the equilibrium temperature of the planet needs to be able to support the existence of liquid water, so the planet requires an atmospheric envelope. Here CHES can directly measure the planetary mass based on relative astrometry, and then define its final internal structure, which is of great significance for assessing the habitability of a planet.

The mass–radius relationship of the discovered exoplanets is a key linkage in defining the model of planet formation and evolution. For low-mass planets, considering the core accretion model of planet formation, it is difficult for them to accrete large amounts of gas; but their mass–radius relationships suggest that some planets' atmosphere-to-mass ratios can vary over a wide range. So, are their larger radius values due to larger initial atmospheric proportions, implying that they are in the early stages of evolution? Therefore, the measurement of accurate planetary mass can help understand the evolution of short-period low-mass planets, and then compare with the observed mass–radius relationship (Figure 5), which can constrain their formation and evolution (Jin & Mordasini 2018). As previously mentioned, CHES will be able to accurately measure the mass and radius of planets, investigate the evolution of a large number of planets, and infer their formation scenarios and material compositions.

2.2.3. Three-dimensional Orbits of Planets and Formation

The mass and three-dimensional orbit of multiple planetary systems are directly related to the origin and evolution of these systems. The finding of exoplanets in the past two decades has brought us even more cognitive breakthroughs: planetary systems are highly dynamical and constantly changing. The three-dimensional structure of multi-planetary systems increases our knowledge of the origin and evolution of planetary systems, and helps us to statistically understand their migration scenarios and the long-term effects of these dynamical processes on planetary habitability (Liu & Ji 2020). The accurate mass and three-dimensional orbits of a nearby multi-planetary system that CHES will solely be able to provide will be the most precious observational basis, and will greatly expand humans' cognition and theoretical research on planetary systems.

Current theories cannot shed light well on the complex scenarios of planetary formation (Raymond et al. 2006; Mordasini et al. 2009; Chiang & Laughlin 2013; Liu & Ji 2020). However, the CHES mission will offer detailed information on the planetary three-dimensional orbits around nearby bright stars with sufficiently high spatial resolution, and further provide strong constraints on distinguishing planetary formation theories, thereby being viewed as one of the unique contributions of CHES compared with other missions.

2.2.4. Planetary Diversity and Follow-up Observations

A large observational population of exoplanets shows that other worlds around other stars appear to be extremely diverse and quite different from those of our own solar system (Borucki et al. 2010, 2011; Batalha et al. 2013; Gillon et al. 2017), e.g., hot Jupiters, warm Neptunes, super-Earths and rocky planets. CHES will focus on the detection of habitable-zone planets around nearby solar-type stars, and further can coordinate with follow-up ground-based and space-based telescopes to conduct characterization of habitable planets. For example, CHES can conduct joint measurements with high-precision RV instruments such as the future E-ELT (Macintosh et al. 2006) and TMT (Skidmore et al. 2015), and can also verify habitable planet candidates discovered by the RV, and can accurately characterize planetary masses and orbital parameters.

Due to the limitation of angular resolution, the most suitable planetary systems for atmospheric characterization by direct

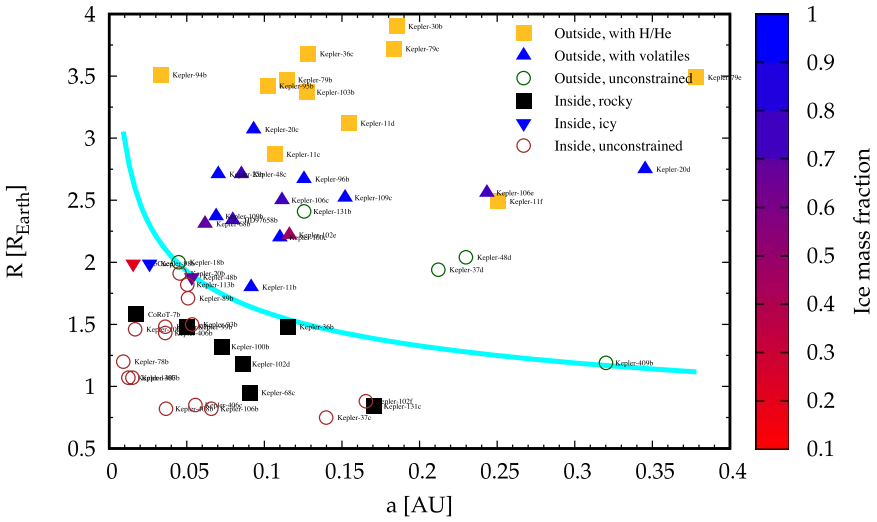

Figure 5. The composition of a planet with its structure and evolution (Jin & Mordasini 2018).

imaging to obtain spectra are located around nearby stars (Gaudi et al. 2020), and the target of CHES happens to be close to nearby Sun-like stars. CHES will discover unknown planets in the habitable zone of nearby stars. Combined with follow-up RV observations and photometric measurements, the masses and orbital parameters of these planets will be accurately determined, and they will be ideal targets for the next generation of flagship space telescopes via direct imaging for deep spectroscopic observations (Gaudi et al. 2020).

2.3. Science Objective Extended: Cosmology, Dark Matter and Black Holes

Besides the detection of terrestrial planets in the habitable zones, CHES will find the member stars for satellite galaxies. High-precision measurements of proper motion will provide strong constraints on the mass of the Milky Way and the properties of dark matter particles. Furthermore, CHES may detect the masses of neutron stars through measuring binary orbital motion to constrain the composition and equation of state. Additionally, CHES will measure the proper motion of black hole binaries to understand the orbit and formation scenario. Finally, CHES will carry out cosmological distances measurement.

3. Scientific Requirements

3.1. Decomposition of Detection Requirements

3.1.1. Positioning Accuracy Requirements

The major scientific objective of CHES aims at the habitable planets orbiting nearby solar-type stars, whose requirements for positioning accuracy are well constrained by this detection.

The detection accuracy is required to be 1 μas for a planet with the same mass and orbit as the Earth at a distance of 3 pc (about 10 light years) from the Sun. It also needs to reach 0.3 μas for detecting terrestrial planets (see Section 4.1 for details) in the habitable zone at 10 pc. To determine 12 parameters of a planet and its host star (including seven planetary parameters and five stellar parameters), we need to observe at least 12 sets of data in 5 yr.

In actual detection, each set of observations is obtained by multiple exposures over 2 hr. Hence, increasing the number of observation groups can obtain a higher signal-to-noise ratio (SNR) or appropriately reduce the detection accuracy requirements. In order to find terrestrial planets in the habitable zone located at 10 pc (about 32.6 light years), when the number of observation groups reaches 200, the required single-observation accuracy must be better than 1 μas.

It is necessary to analyze the primary errors that may affect the detection accuracy to achieve the detection accuracy of 1 μas with each measurement for CHES. Figure 6 depicts the block diagram of top-level error budget and the major composition to the overall budget. Preliminary analysis suggests that the dominant factors influencing the detection accuracy with one measurement include the astrometric errors of target star and reference stars, telescope measurement error, detector calibration error and other errors. Taking into account the overall error budget and current implementation capability of the payload, the major terms of each error weighing factor are 0.35 μas for the target star, 0.58 μas for the reference star, 0.36 μas for the telescope, 0.74 μas for detector calibration and 0.24 μas for other errors.

The main sources of errors in the payload are telescope wave aberration error, residual error after distortion calibration, and detector calibration error excluding the astrometric error

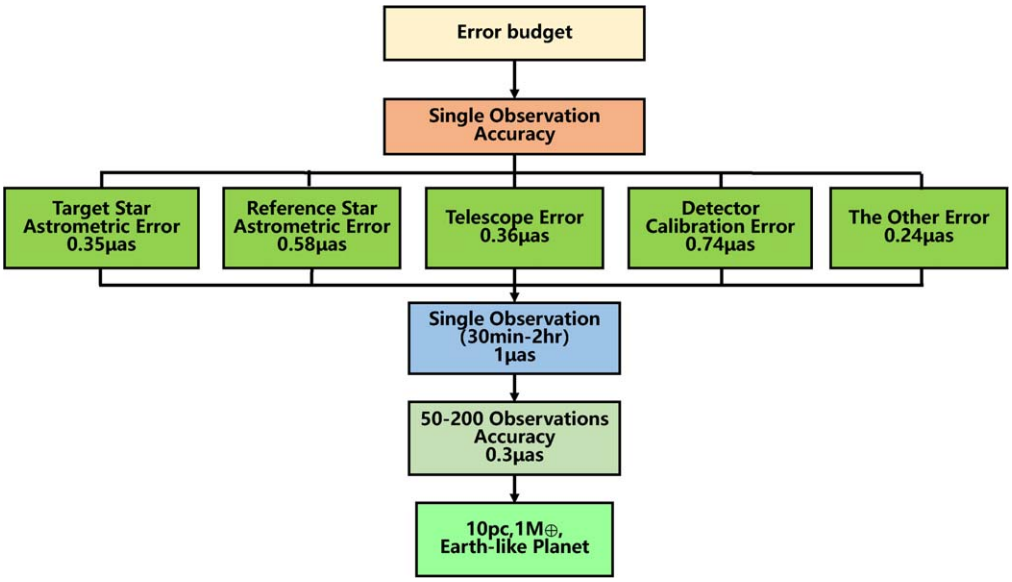

Figure 6. Error budget and analysis of CHES observation accuracy.

between the target star and the reference star. The simulation analysis indicates the requirements for the telescope imaging quality, distortion calibration and detector calibration are as follows to satisfy the corresponding error distribution: the telescope wave aberration is not greater than $\lambda/12$; the residual error after the maximum FOV relative distortion calibration is not less than 0.36 μas; the detector calibration residual is not more than 0.74 μas.

3.1.2. Aperture Requirements

The telescope aperture depends on the effect of photon noise on positioning accuracy. The magnitude of the selected reference star must not be less than 13. Therefore, according to the estimation of the aperture of the CHES primary mirror of 1.2 meters, a star with a brightness of 13th magnitude will receive about 1.6×10^9 photons after 2 hr exposure. In the case of observing eight reference stars simultaneously for 2 hr, the error caused by photon noise is about 1 μas $((\lambda/2D)/\sqrt{8N})$. In the mission, roughly 50–200 observations for each target star should be accumulated in 5 yr, and the equivalent precision is 0.05 μas in right ascension (R.A.) and declination (decl.), corresponding to a signal with an intensity of 0.3 μas that can be measured, where the SNR ≈ 6 (Brown 2009). Therefore, it is decided to select the diameter of the CHES telescope as 1.2 meters after comprehensively considering the existing domestic mirror processing ability, cost, weight, photon noise and other factors.

3.1.3. Focal Length Requirements

The requirement for the focal length of the telescope is based on the diffraction limit of the telescope and the Nyquist sampling theorem. The primary mirror diameter of CHES is 1.2 m. At the observation wavelength of 500 nanometers, the corresponding full width at half maximum (FWHM) of the point spread function (PSF) is about $0\farcs086$. If the focal length of the telescope is 36 m, the FWHM of the target star image on the sCMOS detector is 15 μm. The pixel size of the CMOS detector to be selected is 6.5 μm, which satisfies the Nyquist sampling theorem. The simulations show that a star image size of 32×32 pixels can be in line with the accuracy requirements.

3.1.4. Field of View Requirements

CHES achieves high-precision positioning mainly by measuring the relative position between the target star and the reference star. At least six to eight reference stars are required to enter the CHES FOV. According to the statistics of candidate observation targets, the FOV is greater than $0\fdg44 \times 0\fdg44$. All target stars having at least six $\sim$ eight reference stars can be achieved, which is in agreement with the number of reference stars required for positioning.

3.1.5. Requirements of Interstellar Distance Measurement Accuracy

Since the pixel size of the detector is 6.5 μm and the focal length of the telescope is 36 m, the angular displacement corresponding to one pixel of the detector can be calculated to be $0.037''$. If the measurement accuracy of the distance between stars of 1 μas is to be achieved, the relative positioning accuracy needs to reach 2.7×10^{-5} pixels.

4. Proposed Payload

4.1. Measurement Principle

The major scientific objective of CHES aims at detecting the habitable planets orbiting nearby solar-type stars via unveiling the very tiny periodic signals in the position of the central star induced by the surrounding planets. By measuring the small change and dynamical perturbance of the center position of the target star relative to each reference star (at least six-eight reference stars for each target star), CHES will detect planets with different masses and periods around the target stars. High-precision astrometry is much less affected by stellar surface activities than other observation methods (Shao & Nemati 2009), so high-precision astrometry is the best way to find terrestrial planets in the habitable zone around F, G and K-type nearby stars, but ground-based high-precision astrometry cannot be carried out due to Earth's complex precession-nutation and the influence of atmospheric refraction. Thus, CHES is likely to achieve astrometric precision of micro-arcsecond in space.

The astrometry amplitude α caused by the planet around the target star can be expressed as

$$\alpha = 3\left(\frac{M_p}{M_\oplus}\right)\left(\frac{a_p}{1\,\mathrm{au}}\right) \times \left(\frac{M_*}{M_\odot}\right)^{-1}\left(\frac{D}{1\,\mathrm{pc}}\right)^{-1}\mu\mathrm{as}, \quad (1)$$

where M_p and a_p are the mass and semimajor axis of the planet, respectively. M_* and D are, respectively, the mass of the star and the distance from Sun. For an Earth-mass planet at 1 au around a solar-type star at 10 pc, the astrometry amplitude α is 0.3 μas. Thus, to detect Earth-mass planets, CHES will employ the laser interferometric calibration method, which can improve the relative positional accuracy of stars over the images up to micropixel level.

4.1.1. Target Stars

The CHES project has preliminarily completed the selection of 100 F, G and K types of nearby stars as primary targets of the space mission. The distribution in the celestial sphere is displayed in Figure 7, where the colors represent the types of target stars (e.g., F, G, K) and all stars are within 10 pc from the Earth. In addition, a portion of the samples of selected target stars is summarized in Table 1, where the stellar name, spectral type, distance and magnitude, along with the number of reference stars with respect to each target are listed.

4.1.2. Reference Stars

The reference stars used by CHES are mostly K-type stars with a distance of at least 1 kpc. Typical values for their proper motion and parallax are 1 mas yr^{-1} and 1 millisecond, respectively. CHES is designed to observe the target star with an accuracy of 1 microarcsecond, so the motion of the reference star needs to be considered. However, the distance of the reference star is much larger than that of the target star (average 10 pc), and the potential planets of the reference star have at least 100 times less influence on the observation than the target star. It is only possible for Jupiter-mass planets to affect the measurement of planetary parameters around target stars. Statistically, only 10% of stars have Jupiter-like planets (Nemati et al. 2020). After obtaining observations, those reference stars which have Jupiter-like planets can be first identified, and then can be removed from the list. In addition,

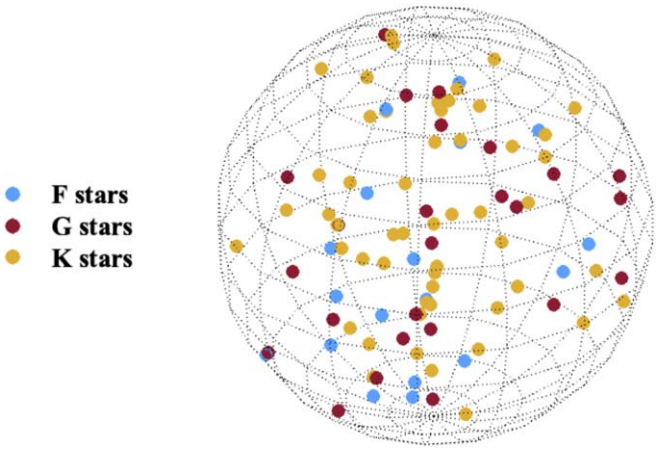

Figure 7. Distribution of CHES target stars within ~10 pc.

Table 1
Examples of the F, G and K Target Stars and Number of Reference Stars

HIP	Name	V mag	Spect.	Dist.	Ref. Stars
		mag	Type	pc	No.
71683	α Cen A	0.0	G2V	1.34	26
71681	α Cen B	1.4	K1V	1.34	48
108870	ϵ Ind	4.7	K5V	3.6	9
96100	σ Dra	4.7	K0V	5.8	14
3821	η Cas	3.5	G0V	6	24
22449	π 3 Ori	3.2	F6V	8	16
1599	cTuc	4.2	G0V	8.6	10
27072	γ Lep	3.6	F6V	9	20
105858	γ Pav	4.2	F9V	9.2	12
14632	ι Per	4.1	G0V	10.5	20

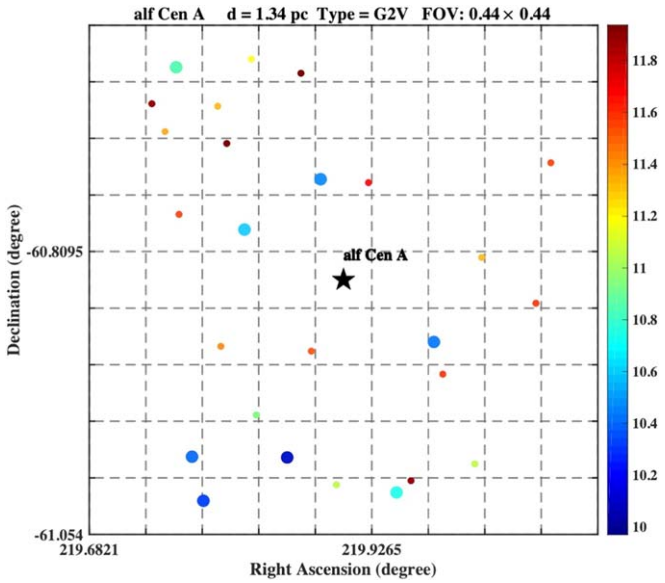

Figure 8. An example of the target star α Cen A with its reference stars.

ground-based RV measurements can also be used to find and eliminate reference stars with Jupiter-like planets.

Stellar activity (spots and bright structures) changes the luminosity of a star over time, affecting the detection of planets. At a distance of 10 pc, the position measurement error caused by stellar activity is much smaller than that induced by terrestrial planets in the habitable zone. For CHES, the criterion to select a reference star corresponding to its activity index is less than -4.35.

An example of target star α Cen A, along with 26 possible reference stars within the FOV ($0.^{\circ}44 \times 0.^{\circ}44$), is presented in Figure 8, where the color represents the magnitude of reference stars while the larger eight circles suggest our preferred reference stars.

4.1.3. Orbital Retrieval Simulations

The motion of the star projected on the celestial sphere is described by five parameters (two position parameters, two proper motion parameters and one parallax parameter), and the influence of any planet on the star is determined by seven parameters (the mass, orbital period, pericenter, orbital eccentricity, orbital inclination and two other angular parameters), so the projected motion of a star with p planets on the celestial sphere can be determined by $m = 5 + 7p$ parameters. For a star harboring three planets, the number of unknown parameters to be determined is 26, and 200 measurements are required to determine the parameters of the planetary system.

Figure 9 shows the simulations of astrometric detection of two types of terrestrial planets with 200 CHES measurements (each corresponding to 1 μas astrometric precision for 2 h), where the top panels correspond to a detection of a three Earth-mass planet at 1 au around a Sun-like star at 5 pc (easy detection), whereas the bottom panels refer to a detection of one Earth-mass planet at 1 au around the star at 10 pc (hard detection). The solid lines in the left and middle columns stand for the projected orbits (R.A. and decl. values) of the terrestrial planets after deriving their parameters, while the peak of the profiles in the right columns represent the orbital periods at one year via Lomb-Scargle periodogram throughout the 5 yr mission. The CHES team also developed codes to perform the retrieval of orbital parameters of terrestrial planets via the simulated astrometric data (Jin et al. 2022).

4.1.4. Planetary Occurrence Rate

Based on the exploration of the Kepler released data, an occurrence rate of a rocky planet within the habitable zone is estimated (Traub 2016; Kaltenegger 2017). The occurrence rate of a planet with an Earth-radius in the range of [0.5,1.35] in the habitable zone is roughly 0.66 ± 0.14, 1.03 ± 0.10 and 0.75 ± 0.11, respectively, for F, G and K-type stars. In the set of CHES targets, there are 18 F-type, 25 G-type and 57 K-type nearby stars. According to the above estimation of occurrence rate of habitable planets, CHES will detect roughly 68–91 habitable planets by the end of its 5 yr mission, while the resultant number of detections of planets can increase if considering a broader range of planetary radii and orbital periods for solar-type stars (Zhu & Dong 2021).

4.2. General Description of the Payload and Challenges

The CHES payload is simple in design and consists of three assemblies: the telescope assembly, the camera assembly and the on-orbit calibration assembly. The composition of the entire payload configuration is illustrated in Figure 10.

4.2.1. Instrumental Challenges

The CHES telescope has a 1.2 m aperture and a 36 m focal length. For a camera with a pixel size of 6.5 μm, the corresponding single pixel FOV is $0.''037$ as aforementioned. To obtain the microarcsecond relative astrometric accuracy, the measurement accuracy of the stellar image centroid displacement needs to reach 10^{-5} pixel, which is a major challenge for the instrument.

In order to achieve the microarcsecond relative astrometric precision, three issues should be solved: (1) A telescope with high-quality, low-distortion imaging. Near diffraction-limited imaging is required to provide perfect PSF over the full FOV of the telescope. To correct errors induced by the temporal variation of the shape of the mirrors, it is necessary to perform microarcsecond accuracy on-orbit calibration of the distortion of the telescope; (2) Micropixel accuracy centroid displacement measurement and detector calibration. All effects that may

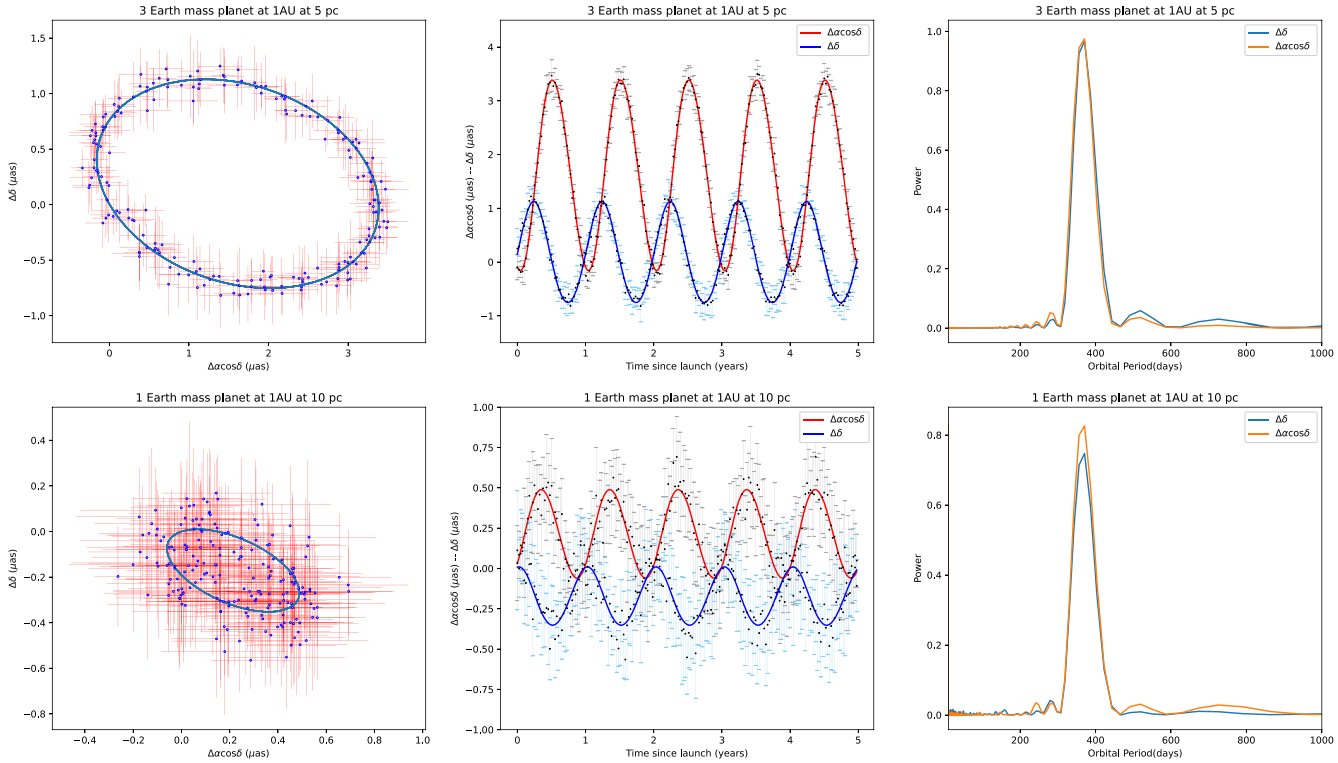

Figure 9. Simulations of astrometric detection of two types of terrestrial planets.

impact the shape and position of the PSF should be considered, such as the geometric stability of the focal plane array (FPA), the photon noise of the stars, and the inhomogeneity of the quantum efficiency (QE) between pixels and within pixels; (3) The satellite needs to maintain ultra-high attitude stability and telescope thermal control accuracy to reach an ultra-high-precision angle offset between the target star and the reference stars.

4.2.2. Instrumental Concept

The CHES payload concept consists of an on-axis TMA telescope with high imaging quality and high stability in the visible band. To obtain the PSF of stellar images for micropixel accuracy centroid displacement measurement, the optical system of the telescope should realize near diffraction-limited imaging. A large focal plane covers a $0.^{\circ}44 \times 0.^{\circ}44$ FOV with a mosaic of detectors. Its dynamic range, frame rate, full well charge and other parameters meet the requirements of observing different magnitude stars in the full FOV. To monitor the mosaic geometry and its QE, a focal plane metrology is performed. While to calibrate the telescope distortions with microarcsecond precision, an on-orbit calibration algorithm based on micropixel accuracy centroid displacement measurement is used.

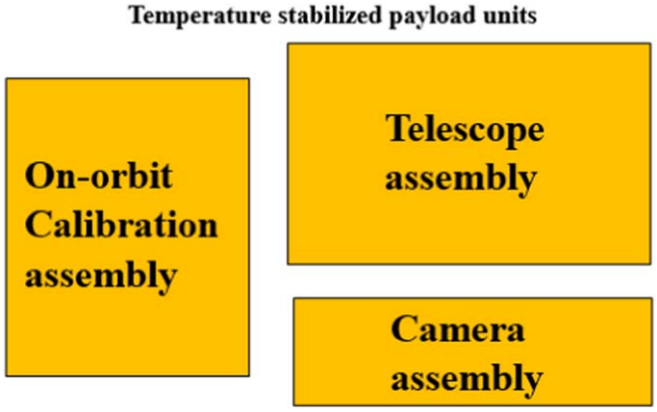

Figure 10. Block diagram of the CHES payload hardware.

4.3. Design of the Payload Subsystems

4.3.1. Telescope Assembly

Considering the demanding image requirements for the PSF and the relative centroid motion due to temporal variations in the positions and shapes of the optics, an on-axis TMA configuration is adopted for controlling the optical aberrations up to third order. It is possible to correct astrometric

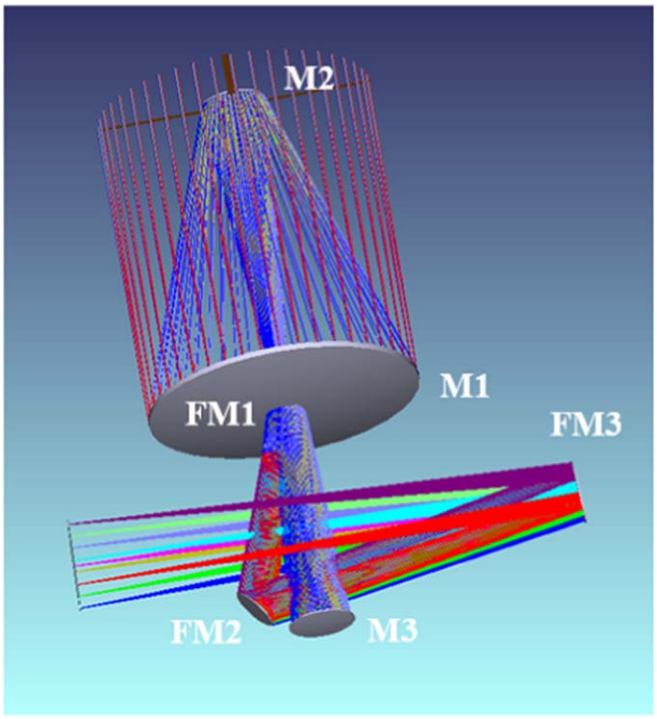

Figure 11. Ray tracing of the CHES telescope.

Table 2
Key Characteristics of CHES Telescope

NO	Specification	Value
1	Aperture	Φ 1.2 m
2	Focal length	36 m
3	FOV	$0.^{\circ}44 \times 0.^{\circ}44$
4	Wavelength coverage	500 nm−900 nm
5	Detector pixel size	6.5μm × 6. 5μm
6	Focal plane size	276 mm × 276 mm
7	Wave aberration	RMS $\leqslant \lambda/12$
8	Distortion after calibration	$\sim 1\mu$as

displacements on the entire FOV. In order to achieve the scientific goals, the key characteristics of the CHES telescope are confirmed as displayed in Table 2.

Figure 11 shows the ray tracing of the CHES telescope. The stars are imaged on the Cassegrain focal plane after passing through the primary and secondary mirrors. The stellar image at the Cassegrain focal plane is re-imaged by mirror M3 and then the final image is formed on the detector by three fold mirrors. It is noted that the first fold mirror FM1 is located near the Cassegrain focal plane. There is a hole in the center of FM1, and the size of the hole is the same as the size of the intermediate image plane. The purpose of the hole is to allow the ray of the intermediate image plane to pass. Due to the hole on FM1, a fraction of the light energy is lost, but there is no loss of FOV. The imaging quality of the designed optical system can be evaluated by spot diagrams, as shown in Figure 12. The results indicate the telescope achieves near-diffraction-limited imaging in the entire FOV.

According to the optical design and thermoelastic effects, the structural design of the CHES telescope is as illustrated in Figure 13.

The mirrors adopt low temperature optimized Zerodur or ultra low expansion glass (ULE) (Westerhoff et al. 2014) and special techniques are used to reduce the weight of the primary mirror (Krödel et al. 2014). To minimize thermoelastic impacts in the position of the mirrors, SiC and TC4 can be adopted for the telescope structure (Verlaan et al. 2012). Aluminum coatings can be used as the optical mirror surface. The total mass of the telescope under consideration of ULE and SiC is estimated to be about 500 kg.

4.3.2. Focal Plane Array Assembly

With the focal length of the telescope of 36 m and the FOV of $0.^{\circ}44 \times 0.^{\circ}44$, the geometric size of the focal plane is about 276 mm × 276 mm. To satisfy the requirements for such a large-format focal plane, a mosaic of detectors will be assembled on the focal plane.

CMOS detectors present a high QE over a larger visible spectral band, faster readout, lower readout noise and better radiation hardness (Marco-Hernández 2020), while CCD detectors have high readout noise in high frame rate readout mode. The existence of a mechanical shutter for a large size CCD will cause vibration in the focal plane, which has an impact on the measurement accuracy of the centroid displacement of stellar images. Here we select a CMOS detector, which can be produced by *Gpixel Changchun Optotech, Inc*. The CMOS chip parameters can be customized to further reach the requirement of the CHES mission. The typical characteristics of detectors required for CHES are summarized in Table 3.

The pixel size of each CMOS chip is 6.5 μm, the number of pixels is 4 k × 4 k , and each size is about 32 mm × 32 mm (including the package size). Thus a mosaic of 81 CMOS detectors is required to achieve full focal plane coverage. The fundamental architecture of the focal plane is depicted in Figure 14.

Considering the consistency with the linear expansion coefficient of the detector packaging material, Invar steel or SiC material is selected as the substrate material; a mosaic of 81 CMOS detectors is fixed to the substrate. To ensure the positional accuracy, geometrical tolerances of the substrate are strictly specified and the processing technology is strictly controlled when the substrate is structurally designed. The position of the detectors is independently detected when

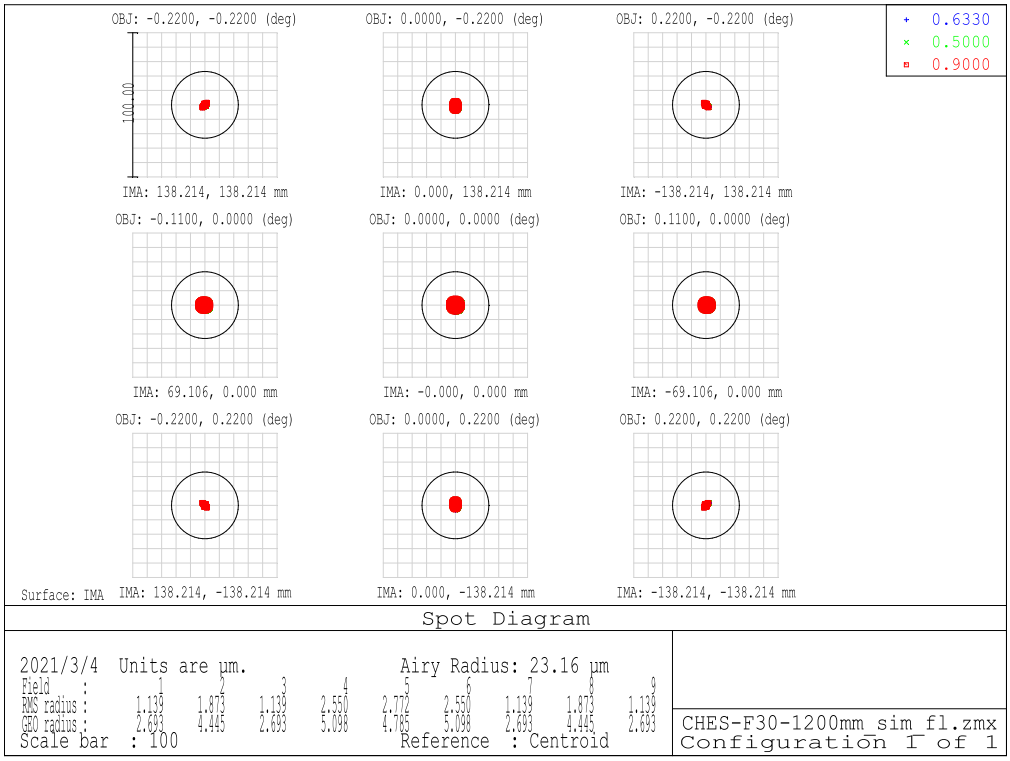

Figure 12. Spot diagrams for the full FOV of the CHES telescope.

Table 3
The Typical Characteristics of Detectors

Specification	Value
Detector size (pixels)	4096 × 4096 pixels
Detector pixel size	6.5 μm × 6. 5 μm
Focal plane size	276 × 276 mm
Pixel scale	37 mas/pixel
Pixel full well capacity	170 ke$^-$
Wavelength coverage	500 nm – 900 nm
QE	>90% (600 nm)
Dark signal (@ − 50°C)	<0.05 e$^-$/pix/s
Readout noise (@10 kHz)	<2 e$^-$/pix

assembling. After the assembling is completed, a high-precision optical measurement is adopted for quality inspection of the mosaic of detectors.

4.3.3. On-orbit Calibration Assembly

The on-orbit calibration assembly consists of an FPA calibration module and a telescope optical distortion calibration module. The calibration mode lasts roughly 2.5 hr and includes 2 hr of optical distortion calibration mode and 0.5 hr of focal plane metrology mode after each 2 hr of scientific exposures. The average scientific exposure is about 2 hr for each target in scientific mode. The CHES satellite enters into calibration mode after 2 hr of scientific exposures. First, a 20 arcsecond dithering is used in the optical distortion calibration mode. The optical distortion calibration mode takes 2 hr of star field integration. The scientific exposures and dither pattern are utilized to calibrate the optical distortion. The optical distortion calibration process is described in Section 4.3.3.2. The 0.5 hr focal plane calibration frames will be taken after the optical distortion calibration mode. The focal plane calibration frames consist of 10 minute single mode fiber Gaussian pattern exposures for the flat-fielding and 20 minute interference fringe exposures for the pixel position calibration. The focal plane calibration is described in Section 4.3.3.1.

4.3.3.1 Calibration of Focal Plane Array.

The FPA calibration subsystem in orbit consists of a module of heterodyne laser interferometry. This module is mainly applied to calibrate the non-uniformity of the pixel positions and inter-/intra-pixel response of the scientific CMOS detector. With the Fourier re-sampling algorithms and the calibrated characteristics of the

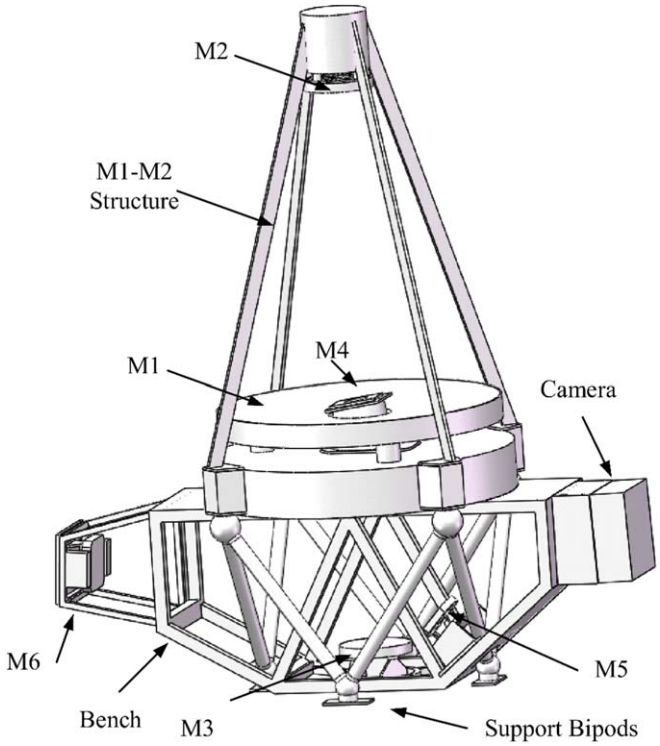

Figure 13. Overall layout of the CHES telescope.

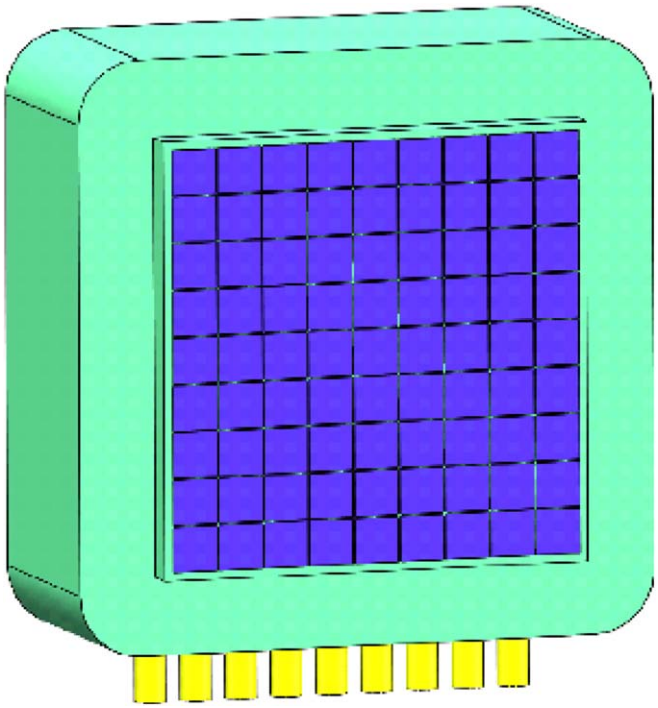

Figure 14. Concept for CHES Camera.

scientific CMOS detector, the micropixel level relative centroiding can be reached on the FPA (Figure 15). It meets the requirements of the CHES mission for the 1 μas measurement accuracy of the angular distance between the target star and the reference star.

The CMOS detector calibration module is mainly composed of six optical fibers. A total of 15 sets of baselines can be obtained by combining them in pairs, so that 15 sets of interference fringes with different orientations and spaces can be formed. These fringes are utilized to calibrate CMOS detectors. The interference baselines and interference fringes are shown in Figure 16.

For an actual detector, the numerical simulation results demonstrate that the centroid displacement measurement accuracy between the target star and reference star can amount to 20 micropixel if we calibrate the higher order terms of the Taylor series of the Fourier transform of the pixel response function, as depicted in Figure 17.

We built a heterodyne laser interferometry and micropixel accuracy centroid displacement measurement testbed (Figure 18), called Laser Interferometric Metrology Testbed (LIMT). We conducted the flat-field response calibration, pixel position calibration, and micropixel centroid displacement estimation with laboratory demonstration based on scientific-grade CMOS image sensors (Figures 19, 20, 21). At present, the centroid displacement measurement accuracy between the target star and reference star (in the artificial star field) can

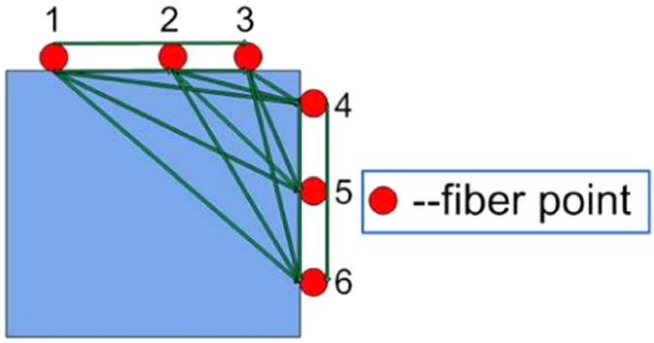

Figure 15. The baselines of the FPA calibration module.

achieve 2×10^{-5} pixel (Figure 22) with flat-field response calibration and pixel position calibration.

4.3.3.2 Calibration of Telescope Optical Distortion.

Static and temporal varying shape errors of the primary mirror will cause a shift in the centroid of the star image, but this shift is common over the full FOV. For relative astrometry, its impact on measurement accuracy is small and negligible (Tan et al. 2022). However, temporal variation of the shape of mirrors after the primary mirror would produce uncommon centroid shifts. Such error will dramatically affect the estimation accuracy. Therefore, the measurement error arising from the variation of the mirror

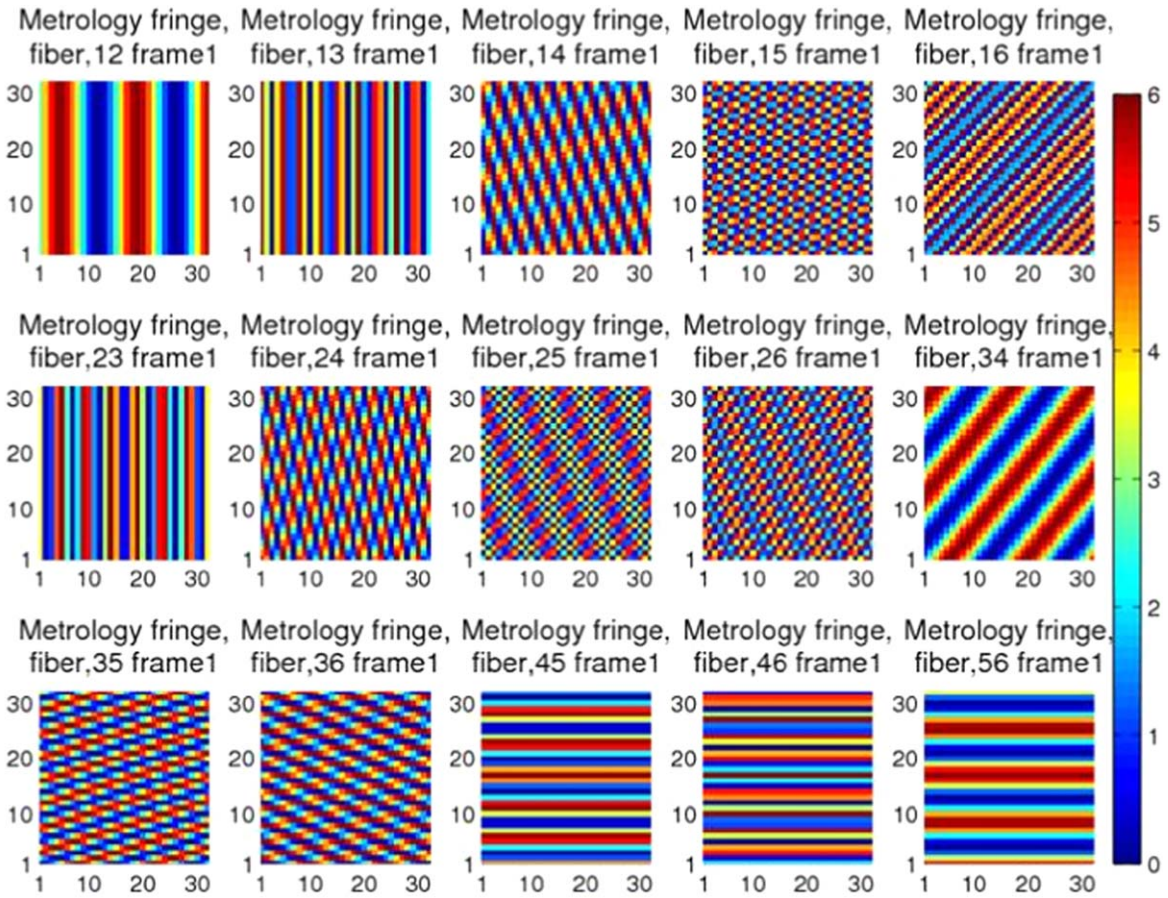

Figure 16. Fifteen sets of interference fringes with various orientations and spaces.

surface shape needs to be calibrated through the on-orbit calibration subsystem.

Multiple independent interferometers can be used to monitor the relative position shift between two mirrors in the telescope, but the monitoring system is extremely complicated and cannot detect the variation of the mirror's surface shape. Therefore, there is no telescope metrology in the CHES payload, but a method to calibrate the star image position affected by the distortion, imaging quality and other relevant factors is proposed and employed. The calibration accuracy arrives at the order of microarcsecond.

The calibration method does not depend on the absolute position coordinates of the stars in the current stellar catalog, but instead uses micropixel accuracy centroid displacement measurement technology and the characteristic of zero distortion of the center FOV of the optical system. Based on the principle of wave front reconstruction in adaptive optics, the on-orbit calibration of the telescope optical distortion with microarcsecond accuracy is realized.

The calibration process is as follows: First, make the pointing direction of the telescope change only in yaw and pitch, and use the micropixel accuracy centroid displacement measurement technology to obtain the displacement of each star image at the center of the FOV and edge FOV. Then, the displacements of the star images in the edge of the FOV and the center of the FOV in the x and y directions are subtracted to obtain the distortion difference and distortion gradient at each star image. The gradient is fitted to obtain the coefficients of the terms in the expression of the distortion gradient function. Finally, the expression of the distortion gradient function is integrated. According to the fact that the distortion at the central FOV of the telescope is zero, the constant term of the expression can finally be obtained and the distortion function is determined, so as to realize the high-precision calibration of the optical distortion of the telescope.

In order to verify the feasibility of the proposed calibration method, a calibration simulation experiment was carried out on the CHES optical system derived from the optical design software. Preliminary results show that, assuming that the measurement accuracy of the centroid displacement measurement is 1 μas, the average value of the distortion residual after calibration is about 1.4 μas.

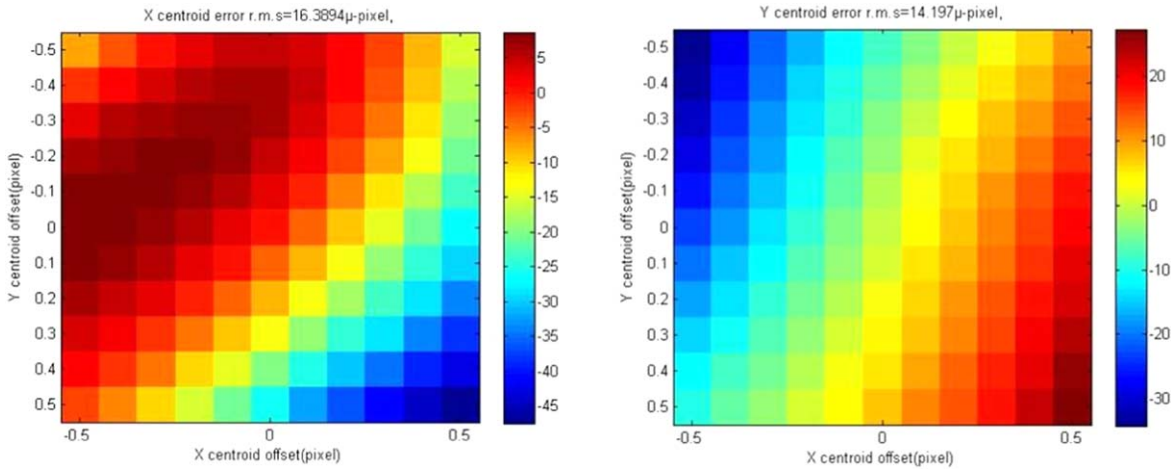

Figure 17. The centroid displacement measurement accuracy between the target star and reference star for *X* and *Y* directions.

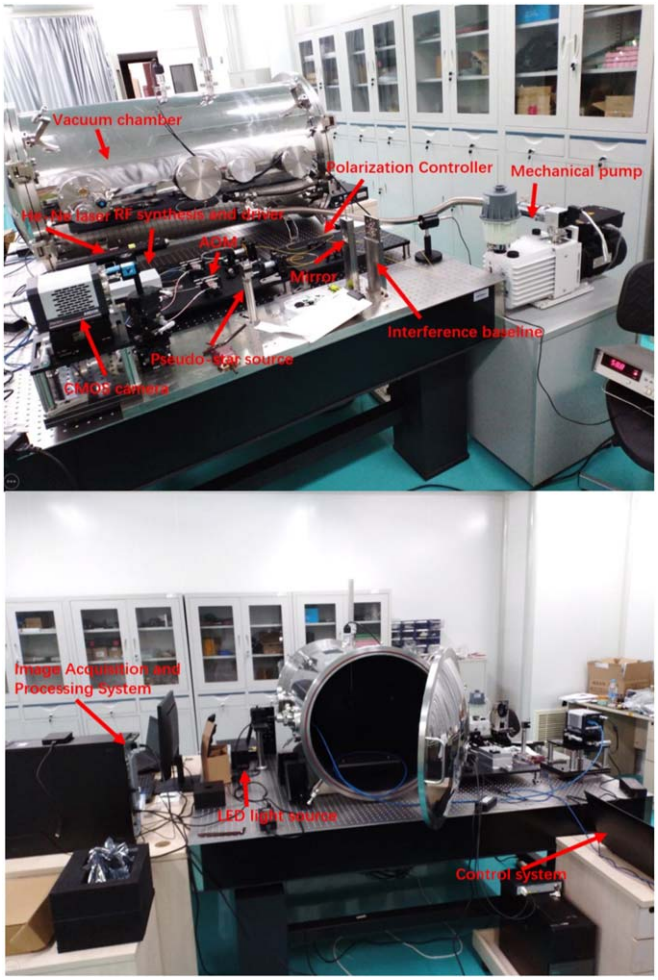

Figure 18. Testbed for heterodyne laser interferometry and micropixel centroid displacement measurement.

Furthermore, we give a graph of the variation of the distortion calibration accuracy with the centroid displacement measurement accuracy under different telescope wave aberration conditions (Figure 23). It can be seen that the calibration accuracy is comparable to the centroid displacement measurement accuracy. If the centroid displacement measurement accuracy reaches submicroarcseconds, the calibration accuracy can also arrive at submicroarcseconds, which meets the requirements of calibration accuracy for the CHES mission.

4.4. TRL Assessment

CHES telescope is based on traditional optical telescope technology, and the key technologies of large-diameter high-image quality telescopes and focal plane splicing can be inherited from the previous programs. To verify the optical performance of the telescope and perform experimental verification of the micropixel accuracy centroid displacement measurement on the telescope optical system, a $1/6$ scale prototype of the telescope has been developed. The scaled prototype bears the same optical structure as the full-aperture CHES telescope, and has identical optical parameters such as F-number, FOV, imaging quality and distortion. The scaled prototype of the telescope includes the primary mirror FM1, the secondary mirror FM2, the tertiary mirror FM3, the front-support, the back-support and the camera (Figure 24). The overall implementation adopts a cuboid structure, and the outer shell is employed to avoid the influence of external stray light. Figure 25 displays the completed $1/6$ scale prototype of the telescope.

The wave aberration of the full FOV of the scaled telescope prototype has been tested, and the test results are shown in Table 4. It can be seen that the wave aberration root mean

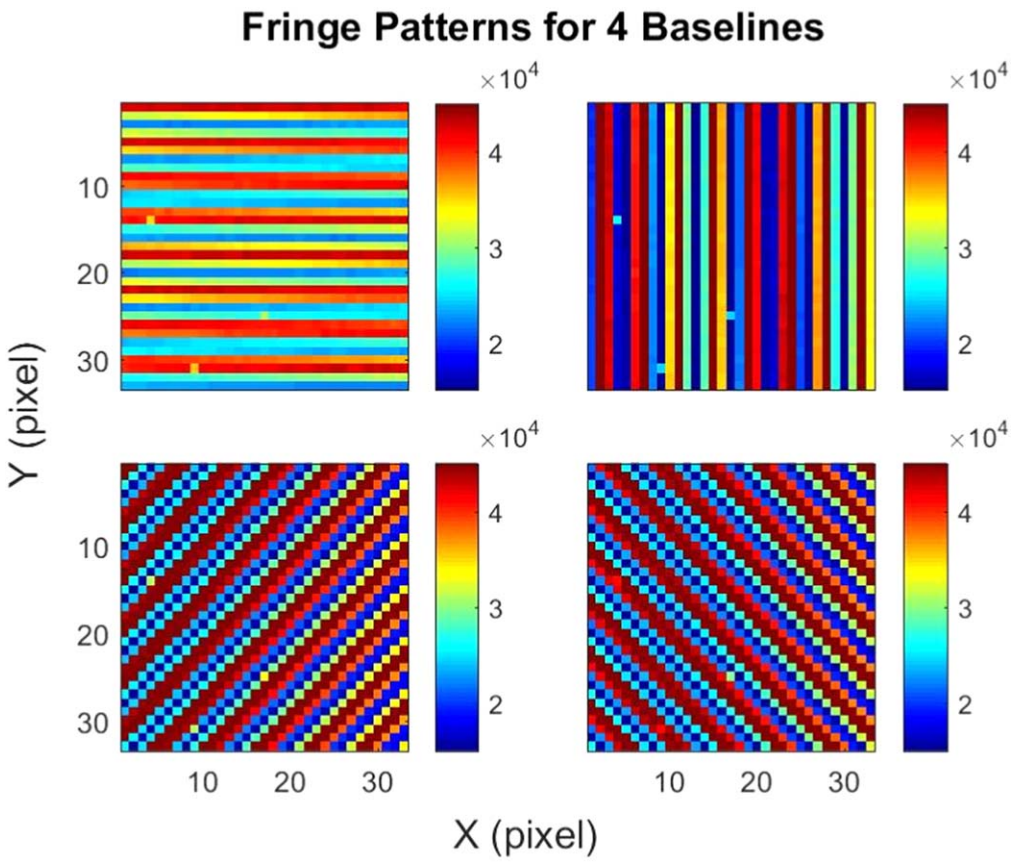

Figure 19. The interference fringe images from the testbed for four different baselines.

Table 4
Test Results of Wave Aberration in Different FOVs of the Scale Prototype

FOV	(0°, +0.22°)	(−0.22°, 0°)	(0°, 0°)	(+0.22°, 0°)	(0°, −0.22°)
RMS	$\sim\lambda/14$	$\sim\lambda/19$	$\sim\lambda/26$	$\sim\lambda/14$	$\sim\lambda/13$

square (RMS) of each FOV is better than $\lambda/13$. Although only a scale prototype is completed, our payload research team is very experienced in the microstresses in large-aperture telescope mirrors and the control of surface shape changes. We have successfully developed a meter-scale large-aperture space-based telescope and on-orbit performance is good. According to the standards for classification and definition of Technology Readiness Level (TRL), the TRL of the CHES telescope technology can attain level 7 (Table 5).

In terms of the mosaic of detector technology, our payload research team is participating in the development of the FPA of the CSST. The effective physical size of the focal plane is about 560 mm × 490 mm, and the focal plane area is about 4 times that of the CHES telescope. At present, the key technologies such as low-temperature flatness detection, self-gravity surface shape variation detection and focal plane surface shape control have been completed, and the surface shape accuracy of the mosaic focal plane meets the requirements of the project. The related technology can be inherited and applied to the focal plane assembly of the CHES telescope. The TRL for the mosaic of detectors can reach level 6.

Table 5
Payload TRL Assessment

Item or Function	TRL	Heritage or Comment
Telescope structure	7	Rich experience in the development of large-aperture space-based telescopes;
Telescope optics	5	Mature TMA optical structure; Scaled prototype has been completed
Mosaic of detectors	6	CSST
On-orbit calibration	5	Laboratory validated, but not to CHES FPA scale.

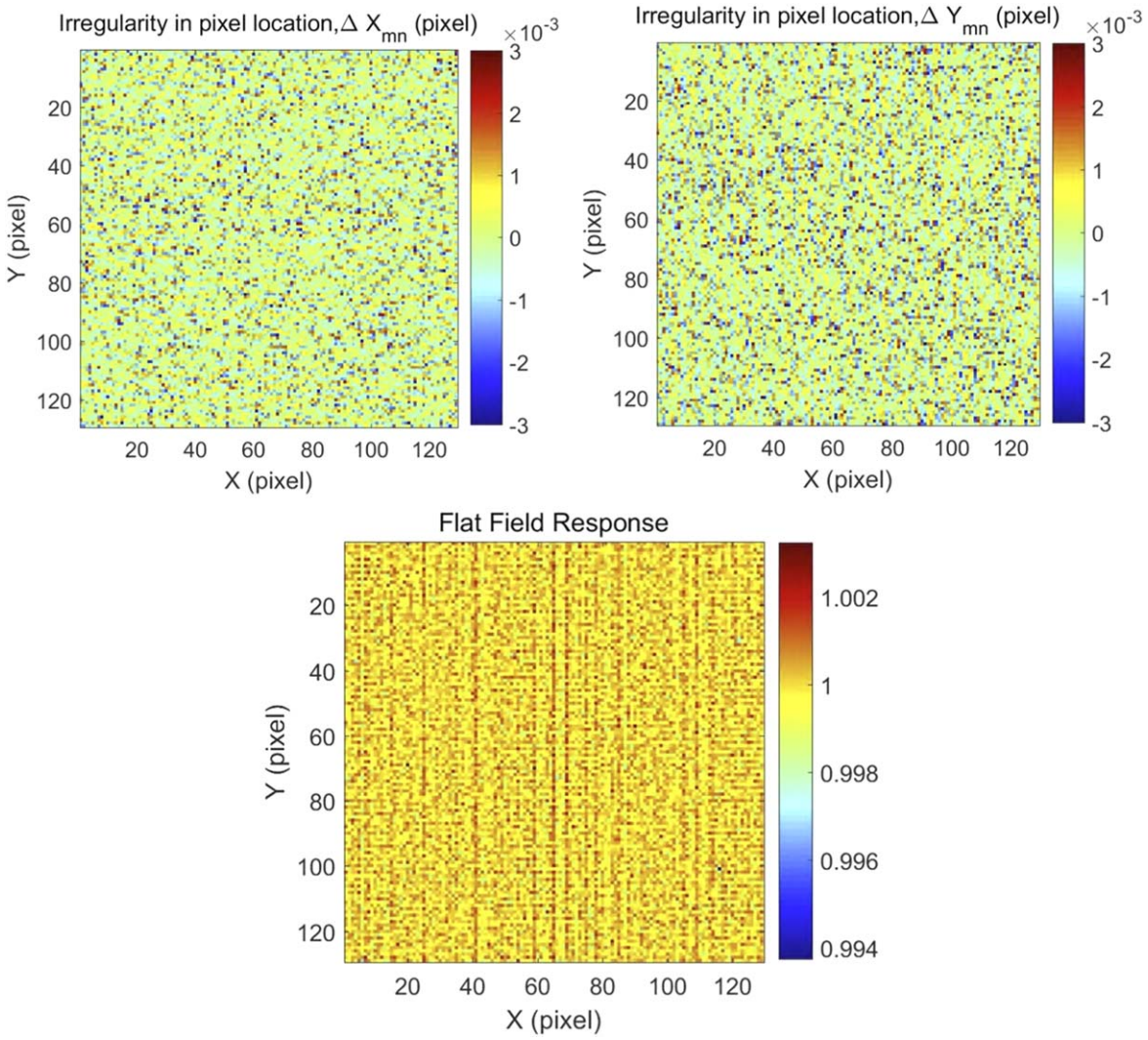

Figure 20. Results of flat field calibration and the pixel position measurements.

An on-orbit calibration testbed was built in a vacuum environment and the experiment of the FPA calibration was carried out. The calibration of micropixel accuracy was laboratory validated. Here the TRL can attain level 5.

5. Proposed Mission Configuration and Profile

5.1. Mission Requirements and Analysis

5.1.1. Mission Requirements

The CHES mission will detect the habitable-zone terrestrial planets orbiting nearby solar-type stars with the aid of the relative astrometric method. Hence, here we design the satellite system with ultra-high attitude stability and thermal control accuracy to meet the requirements of ultra-high-precision centroid displacement measurement between the target star and reference stars. The satellite adopts a 3-axis stabilization zero-momentum attitude control mode, combining telescope payload, star sensor and gyroscope to determine the attitude, and with super-stable structure and thermoelastic control to achieve high accuracy ($0\farcs07$) and high stability attitude control ($0\farcs0036/0.02$ s); the satellite adopts a compartmentalized thermal design and a combination of active and passive thermal control mode. It also adopts *X*-band measurement, control and data transmission integrated design, equipped with 512 Gb large-capacity storage and phased array antenna, to realize the daily 84 Gb of scientific data transmitted at a rate of 20 Mbps. The total weight of the satellite when launched is about 2.93 t, with a peak power consumption of 1493 W, and it is planned to be launched at the Xichang Satellite Launch Center aboard a CZ-3C rocket.

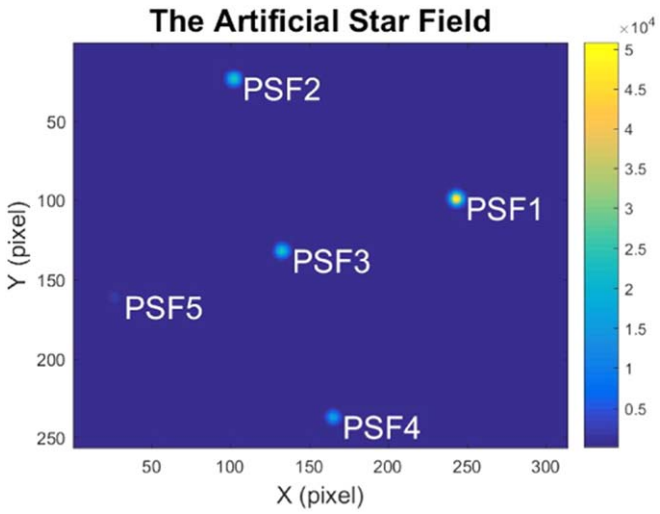

Figure 21. The artificial star field from testbed.

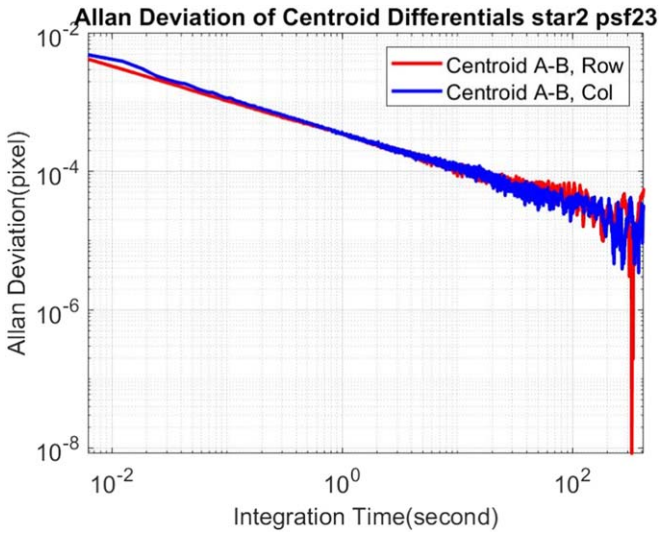

Figure 22. The results for centroid displacement measurements.

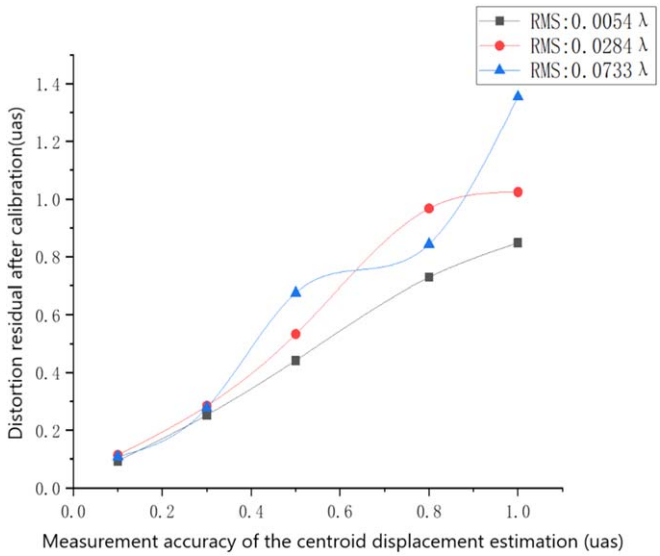

Figure 23. The variation of distortion residual after calibration.

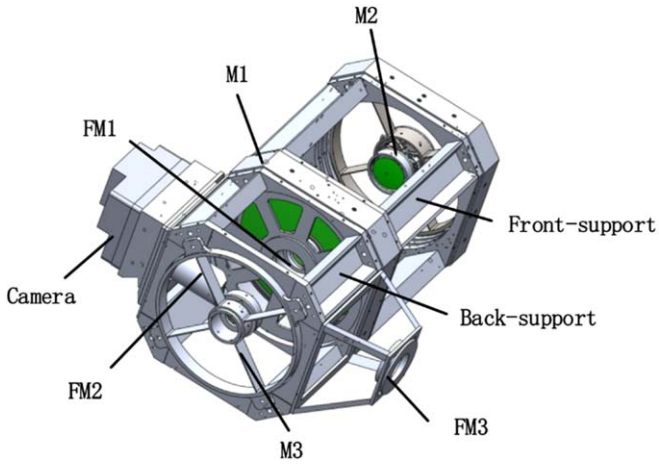

Figure 24. Structure diagram of scale prototype of the telescope.

5.1.2. Mission Orbit

As a satellite for nearby habitable planet detection using microarcsecond relative astrometric measurement, the CHES satellite will have extremely high requirements on attitude stability and thermal control accuracy. By analyzing the solar-terrestrial Lagrange point orbit, geocentric highly elliptical orbit (HEO), Earth-Moon resonance orbit and heliocentric Earth trailing orbit, we find that the solar-terrestrial L2 point orbit has many advantages including being free of the Earth's gravity gradient, which enables all-day scientific observations, and a relatively stable thermal radiation environment. Moreover, China has the capability of delivery, measurement and control, and data transmission to carry out the L2 mission. Thus, the solar-terrestrial L2 orbit is designed as the mission orbit.

5.1.3. Space Environment Analysis

The CHES satellite operates at the solar-terrestrial L2 point where the space environment is mainly the interplanetary space environment, which mainly consists of high-energy radiation, solar wind plasma, ultraviolet radiation, etc. The main effects of these on the satellite are the following four aspects.

(1) Single-particle effect analysis: the single event upset (SEU) rate is slightly higher than that of geosynchronous orbit, and the SEU rate rises by more than 1 order of magnitude during proton events, requiring attention to the impact of single-particle effect occurring in the device.

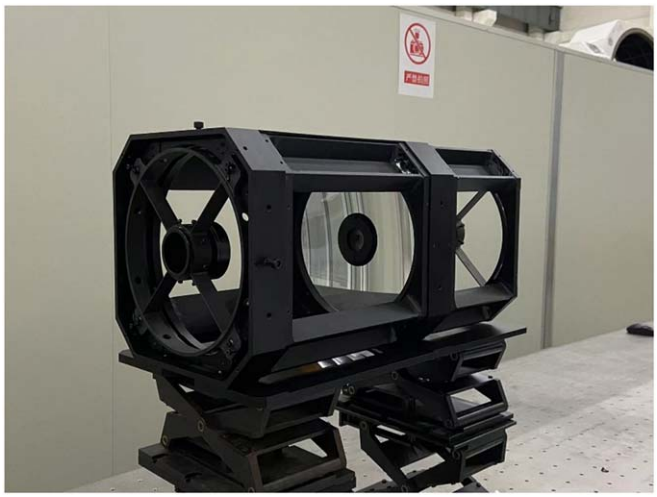

Figure 25. Completed 1/6 scale prototype of the telescope.

(2) Total dose analysis: The dose received under the 3 mm aluminum shield is between 5.5 krad $\sim$ 9. 7 krad in 5 yr.

(3) Displacement damage effect analysis: the impact on CMOS detectors should be considered, and specific devices need to be shielded and reinforced according to their ability to withstand radiation.

(4) Surface charging effect analysis: The test results indicate that the charging effect has little impact on the safety of the CHES satellite.

5.1.4. Thermal Environment Analysis

The CHES satellite, at the solar-terrestrial L2 point, is mainly influenced by solar radiation, as well as thermal radiation from the Earth and the Moon. (1) Solar radiation: the solar constant (the value of the energy flux density in the visible band received per unit area perpendicular to the direction of sunlight per unit time) at point L2 ranges from 1296 W m^{-2} to 1389 W m^{-2}. (2) Earth and lunar thermal radiation: the sunlight albedo energy flow of the Earth is around 0.0004 W m^{-2}, and the sunlight albedo energy flow of the Moon is not higher than 0.0002 W m^{-2}. The infrared radiation energy flow of the Earth and the Moon does not exceed 0.005 W m^{-2}, which has little effect on the satellite.

5.1.5. Access Analysis

CHES operates at the solar-terrestrial L2 point. Due to the requirement of ultra-high attitude stability, the satellite data transmission adopts an X-band phased array antenna. We can use the Kashgar 35 m deep-space station, Argentina 35 m deep-space station, Jiamusi 66 m deep-space station and 40/50 m equipment of Miyun station of Chinese Academy of Sciences for the data reception.

(1) The budget of measurement and control link

CHES is located at the solar-terrestrial L2 point 1.7 million km from Earth. The satellite carries a wide-beam antenna, and the ground relies on a 35 m deep-space measurement and control station. The link margin is 3.05 dB at 2048 bps telemetry rate and 13.52 dB at 2000 bps remote control rate.

(2) The budget of digital transmission link

Take the 35 m Kashgar deep space station with the most demanding reception index as an example, the farthest distance between the satellite and the ground is 1.7 million km, the data transmission rate is 20 Mbps, and the link margin is 3.34 dB when the phased array antenna is used on the star for downlink data transmission.

(3) Visibility analysis

By setting the minimum elevation angle of the ground station antenna at 5°, the coverage arc of the CHES satellite passing through the ground station is simulated and analyzed. The visibility time between the satellite and the three ground stations of Jiamusi, Kashgar and Miyun is between 7.9 and 15.3 hr. The scientific data are about 84 Gb, the information rate is 20 Mbps and the daily data transmission takes about 1.2 hr, which meet the satellite data downlink demand.

5.2. Mission Profile

5.2.1. Launcher and Orbit Injection

5.2.1.1 Launcher. This mission can be launched to the initial orbit using a CZ-3C at the Xichang Satellite Launch Center. (1) Initial orbit requirements: the launch vehicle sends the satellite to a parking orbit with an orbital inclination of 28°.5, a perigee altitude of 200 km and an apogee altitude of 35 958 km; (2) launch capacity requirements: $\geqslant$2930 kg (CZ-3C@GTO has a carrying capacity of about 3.8 t); (3) launch envelope size: $\geqslant$3761 mm $\times$ 6487 mm (including adapters).

5.2.1.2 Orbit injection. According to the mission analysis, the halo orbit of the solar-terrestrial L2 point with Az of 110,000 km is designed. The mission orbit entry parameters are listed in Table 6.

The satellite is put into a parking orbit with an orbital inclination of 28°.5 (200 km $\times$ 35,958 km) by the launch vehicle. The satellite maneuvers in the perigee of the parking orbit and transfers to the mission orbit. The satellite transfers to the halo orbit along the invariant flow pattern, which take about 117 days. When the satellite approaches the halo orbit along the stable invariant manifold, a smaller velocity pulse needs to be applied to bring it into the halo orbit, as displayed in Figure 26. To summarize, the maneuvers during the transfer process include the transfer orbit entry maneuver and the halo orbit insertion maneuver.

Due to the long orbit transfer time of the satellite, it is also necessary to consider the midway correction maneuver to correct the orbit error and ensure the orbit accuracy in the actual flight. The correction required for this process is no more than 150 m s^{-1}. The maneuver required for each orbit

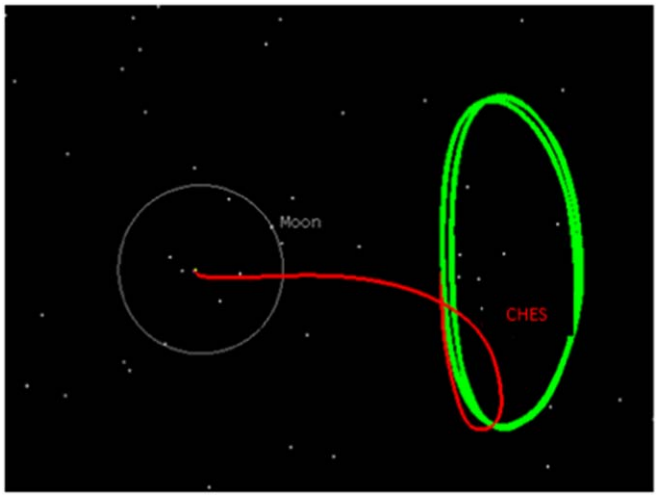

Figure 26. CHES mission orbit.

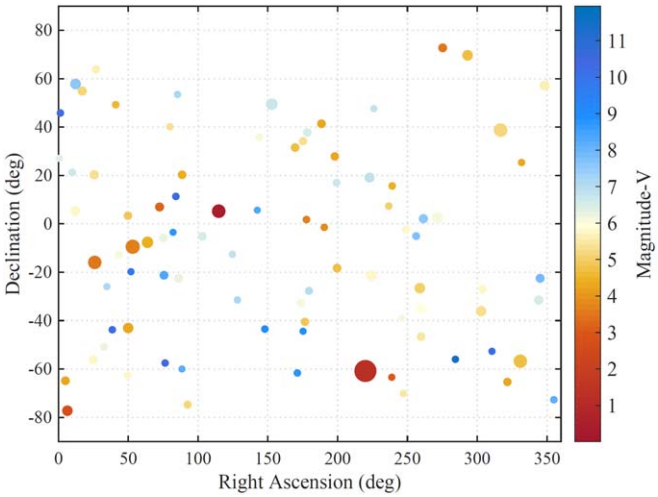

Figure 27. Target star distribution.

maintenance in the halo orbit is about 2 m s^{-1}, and the orbit maintenance period of 90 days can satisfy the mission requirements. In addition, it is also necessary to consider the attitude control fuel consumption and orbital control design margin. The orbit control engine specific impulse is 315 s, and the attitude control engine specific impulse is 215 s. The satellite fuel is required to be 84 kg.

5.2.2. Observing Strategy

5.2.2.1 Observing strategy design. As previously mentioned, the primary scientific objective of the CHES satellite will focus on the discovery of Earth-like planets in the habitable zone around stars within 10 pc, where Figure 27 exhibits the target stars under selection.

Table 6
Mission Orbit Entry Parameters

Orbit injection time	2025/6/1 00: 00: 00.000 UTCG		
Position-X	−408023 km	Velocity X	0.515 501 km s^{-1}
Position-Y	−1132040 km	Velocity Y	−0.174719 km s^{-1}
Position-Z	−371616 km	Velocity Z	−0.0768254 km s^{-1}

According to the distribution of the target stars to be observed by the CHES satellite and the requirement that the solar suppression angle of the telescope is not less than 60°, the observation modes include conventional pointing and revisit pointing. (a) Conventional mode pointing (Figure 28): the telescope optical axis is perpendicular to the Sun–Earth direction and rotates around the Sun–Earth vector to observe the target stars on the coverage sky area in turn, which can reduce the number of satellite attitude maneuvers and improve the observation efficiency. (b) Revisited mode pointing (Figure 29): side-swing observations of the target stars on the left and right sides of the coverage sky area perpendicular to the Sun–Earth. When the Earth revolves around the Sun, all target stars can be covered in six months.

Based on the pointing design, the observation mode analysis of the CHES satellite in mission orbit to detect the target star is carried out. The observation mode of the satellite is described as an example of satellite observation of a target near 60° longitude (Figure 30). The satellite can observe the target near 60° and 240° longitude at the same time with the conventional pointing around the Sun–Earth vector, as shown in the yellow area on the right side of the observation mode schematic. The observation order is from top to bottom or from bottom to top, as depicted in Figure 30. In this case, considering that the solar rejection angle of the telescope is 60 degrees, the satellite can also cover the area of longitude from about 0° to 90° and 210° to 360° by the pendulum measurement, as displayed in the red box on the right side of the observation mode schematic (Figure 31).

5.2.2.2 Observing Efficiency Analysis. The main events of the CHES satellite in mission orbit include: scientific observations, communication between the satellite and the ground station, charging of the battery, attitude maneuvering and high stability pointing attitude control for the satellite to observe different targets. The preliminary analysis allows for about 16 hr of scientific observation per day, so the total scientific observation time is about 29,200 hr during the 5-year lifetime.

5.3. Spacecraft Preliminary Design

5.3.1. Spacecraft Subsystems Overview

The CHES spacecraft consists of a satellite platform and payload. The satellite platform mainly consists of structure, thermal control, electrical and power supply, telemetry,

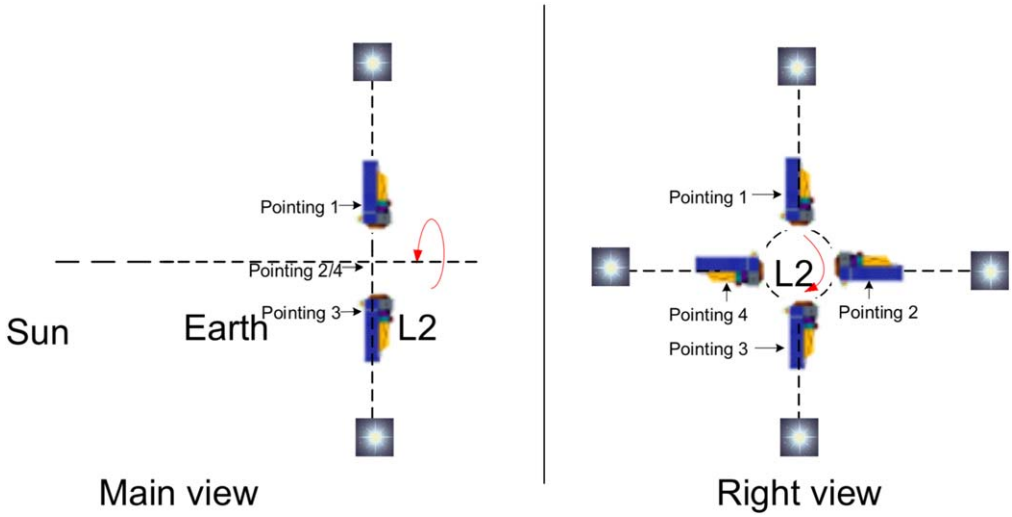

Figure 28. CHES conventional mode pointing diagram.

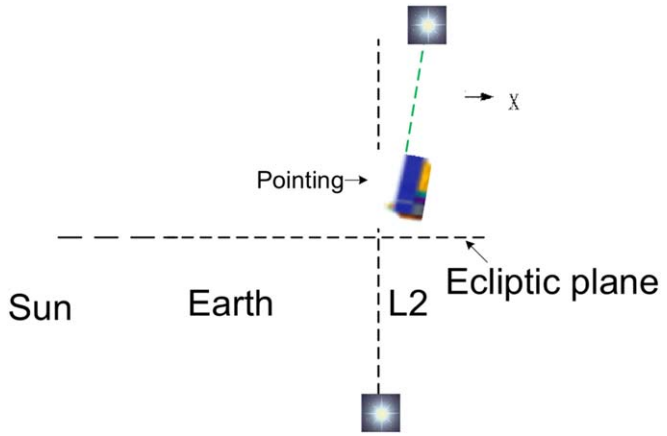

Figure 29. CHES revisited mode pointing diagram.

tracking and control (TT&C), data transmission, attitude and orbit control (AOCS), satellite management unit (SMU), providing energy, communication, thermal control and other operations for the payload. The payload is an optical telescope. The composition of the CHES spacecraft is illustrated in Figure 32. The main technical indicators of the satellite are given in Table 7.

5.3.2. System Preliminary Scheme Overview

5.3.2.1 Structure and accommodation. The concept behind the CHES satellite adopts the idea of compartmentalized design. The whole satellite consists of three parts: the service module, the propulsion module and the payload module (see Figure 33). The telescope payload is mounted on the optical reference plate and supported by carbon fiber support rods to form the payload module. The optical reference plate and the support rods are fastened, and the carbon fiber layup design is used to improve the force thermal stability of the payload module. The service module has a framed panel configuration with hexagonal columns for mounting most of the on-board units. The propulsion module is laid out below the service module. The load bay is connected to the service bay main frame by six titanium bearings to shorten the force transfer path. The two modules are insulated to improve the thermal stability of the payload during observation. The satellite contains one $-X$-plane, $\pm Y$-direction fixed solar wings, both insulated.

5.3.2.2 AOCS. The satellite uses a three-axis stable attitude control method. The composition of the attitude orbit control system is as diagrammed in Figure 34.

The working modes of the AOCS subsystem are divided into the entry phase (after separation of satellite and rocket), orbit transfer phase, mission orbit entry phase, mission phase and safe mode. The transition flow between modes is illustrated in Figure 35.

The payload requires satellite pointing accuracy of ($0\farcs07$) and attitude stability control of ($0\farcs0036/0.02$ s). To achieve this high precision and high stability pointing, the satellite attitude pointing information is first measured using a high precision star sensor and gyroscope, and the satellite attitude is controlled using a 20 mN cold gas thruster to achieve the initial target pointing capture stable state of the telescope. Then, the reference star positioning information output from the telescope is used as the tracking target, and the μN level thruster is utilized as the actuating component for high-precision attitude pointing stability control to achieve the attitude accuracy and stability requirements for the final requirements of multiple

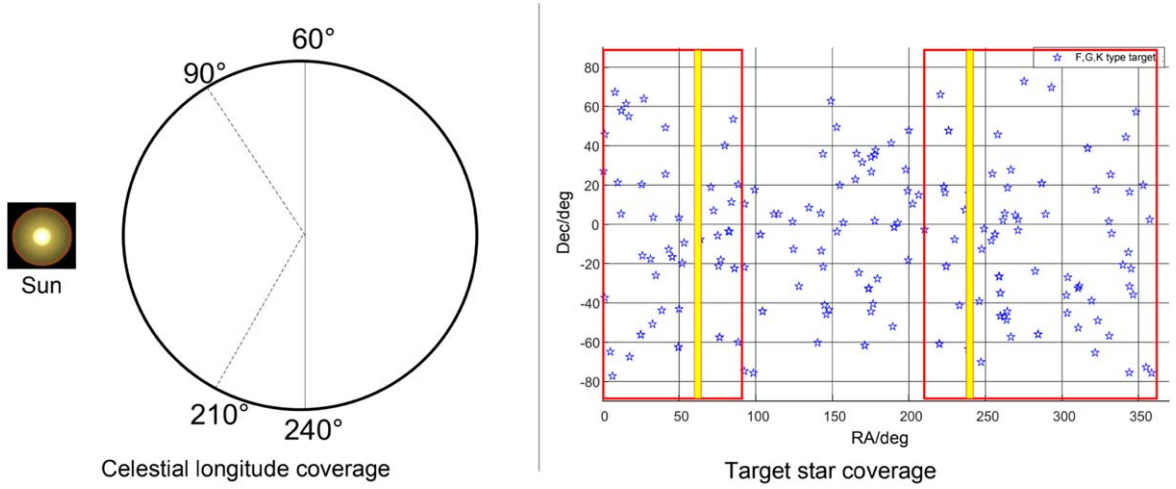

Figure 30. CHES observation mode diagram.

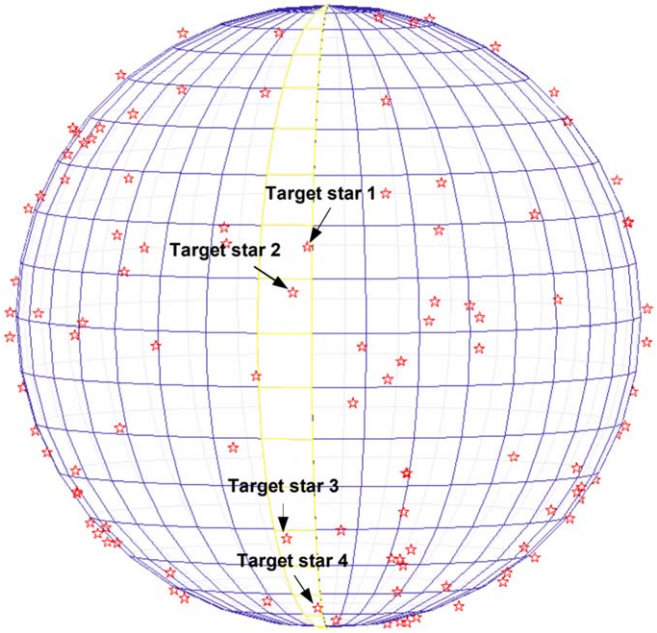

Figure 31. CHES observation sequence diagram (sequence for target stars is 1 −> 2 −> 3 −> 4).

mission observations of the same target. The control flow chart is drawn in Figure 36.

5.3.2.3 Thermal Control. The satellite adopts a thermal control scheme combining active thermal control and passive thermal control. The temperature of the satellite platform unit is controlled in the range of -15° C $\sim 45^\circ$ C. The unit layout is designed to keep the heat-generating unit as far away from the telescope's heat-sensitive components as possible, and the nearby units should operate at a constant power consumption as much as possible during the load observation period. The telescope has an extremely high temperature control requirement, and is installed with the satellite insulated with a special thermal control design (Figure 37); the scheme is as follows.

(1) Telescope external temperature control scheme. The telescope is designed with a 3 mm aluminum alloy surrounding structure on the outside of the telescope as a secondary temperature control object, and the temperature is controlled by a heater with a temperature control stability of $\pm 0.5^\circ$ C. As a first-level temperature control object, the telescope body is heat exchanged with the surrounding structure by radiation.

(2) The internal temperature control scheme of the telescope. A radiation plate is added between the two primary mirror components to compensate for the heat dissipation from the primary mirror to deep cold space. A second-level temperature control structure is installed on the outside of the secondary mirror to compensate for the radiation temperature of the secondary mirror. Graphite strips are attached to the truss supporting the secondary mirror to reduce the temperature gradient of the truss.

(3) Focal plane detector box temperature control scheme. The focal box is equipped with a large heat sink to reduce the temperature variation; the focal box is insulated from the telescope body; a loop heat pipe is used to connect the external radiation heat sink to dissipate the heat and a loop heat pipe with a heat transfer power of more than 800 W is selected.

Thanks to the solar-terrestrial L2 halo orbit and the anti-Sun pointing, the external flux is quite stable after shielding from the solar heat flux. Heat leak from the aperture is certain and is compensated by the heaters. The telescope structure is heat insulated and utilized as the second stage control unit, including the telescope cavity and the lower part of the baffle, to maintain the temperature $\pm 0.2^\circ$ C. The mirror is heated through radiation by the bracing structure, which is the first stage control unit. Also there are heaters on the mirror with power level of milliwatt to keep a uniform temperature. The

Table 7
CHES Main Technical Indicators

Item		Technical indicator
Mass	Launch	2930 kg (CZ-3C@GT0 launch capability about 3.8 t)
Size		ϕ 3761 mm × 6487 mm
Thermal control	Method	Combination of active thermal control mode and passive thermal control mode
	Telescope optical system	Working temperature $20 \pm 5^{\circ}$ C, Temperature stability 45 mK
	S/C platform, Other parts of the telescope	-15° C $\sim +45^{\circ}$ C
Power	Solar cell array	11.8 m^2 triple junction GaAs battery array
	Battery	120 Ah Lithium ion battery
	Bus voltage	30 ± 0.5 V
Attitude control	Method	Three-axis stabilization
	Pointing accuracy	$0''.07$
	Pointing stability	$0''.0036/0.02$ s
Propulsion	Thruster	attitude control thruster: 12^{*} (1 μN $\sim$ 50 μN) ; Attitude control microthruster: 12^{*} 20 mN ; orbit control engine: 490 N + 12^{*} 10 N ;
	Propellant	Propulsion module: 840 kg; Service module: 150 kg;
Telemetry	Telemetry code rate	512 bps, 2048 bps, 4096 bps, 8192 bps
	Telecontrol code rate	500 bps, 1000 bps, 2000 bps
Data transmission	Working frequency band	X
	Modulation mode	QPSK
	Information rate	20 Mbps
	Storage capacity	512 Gbits
	Reading and writing ways	Write in file order and read randomly
SMU	CPU	AT697
	Basic frequency	80 MHz
	PROM	128 KBytes
Launch vehicle and spacecraft interface	Connection and separation mode	Wrapping belt
	LV and S/C connecting ring	Φ 1194 mm
Longevity and Reliability	Longevity	5 year
	Reliability	End of life better than 0.65 (TBC)

essential way of temperature control is multi-stage technology and we have made some improvement from Taiji-1, which can be applicable to the CHES telescope.

5.3.2.4 Energy. The satellite adopts a fully regulated bus with a voltage range of 30 ± 0.5 V. The solar array adopts a triple junction GaAs solar cell with solar sail area of 11.8 m^2 and final output power of 1493 W. A 120 Ah battery pack is selected for the Li-ion battery pack.

5.3.2.5 Communications. The CHES satellite deep space communication adopts an X-band measurement and control/digital transmission integrated communication scheme. Since the CHES satellite has extremely high requirements for attitude stability, a phased array antenna is selected for data transmission in order to avoid the impact of satellite attitude adjustment or vibration generated by the turntable on the load observation. The measurement and control are carried out by a wide-beam omnidirectional antenna with a multi-tone system and a function of sending DOR beacon signals.

5.3.2.6 SMU. SMU consists of hardware and software; the hardware is the housekeeping computer and the software is the housekeeping software. The housekeeping computer uses a dual processing system, a centralized management scheme and keeps dual cold backup. The software adopts the embedded real-time operating system VxWorks, with different application software.

5.3.3. Budgets

(1) Mass budgets

The CHES satellite mass allocation is expressed in Table 8. CHES satellite's dry mass is 1558 kg, including 990 kg of propellant, and the total mass is 2930 kg (including a 382 kg margin).

(2) Power budgets

The CHES satellite power allocation is listed in Table 9.

Since the payload, thermal control, TT&C, data transmission and AOCS are not in the peak working state at the same time, the satellite's peak power is 1493 W instead of 2393 W.

5.3.4. Evaluation of Key Design Challenges

5.3.4.1 High stability attitude control. Satellite high stability attitude control is the key technology of the satellite. Technology inheritance: (1) precision guidance technology, based on the design of the Space Variable Objects Monitor (SVOM) satellite FGS, the SVOM satellite has completed development of Gaia-based FGS electronic star map simulator, and implemented semi-physical simulation verification test.

SVOM is planned to be launched in December 2023. (2) Highly refined closed-loop control technology, based on the development of μN level thrusters and the study of high stability control algorithms, was already conducted on the Taiji-1 satellite launched in September 2019.

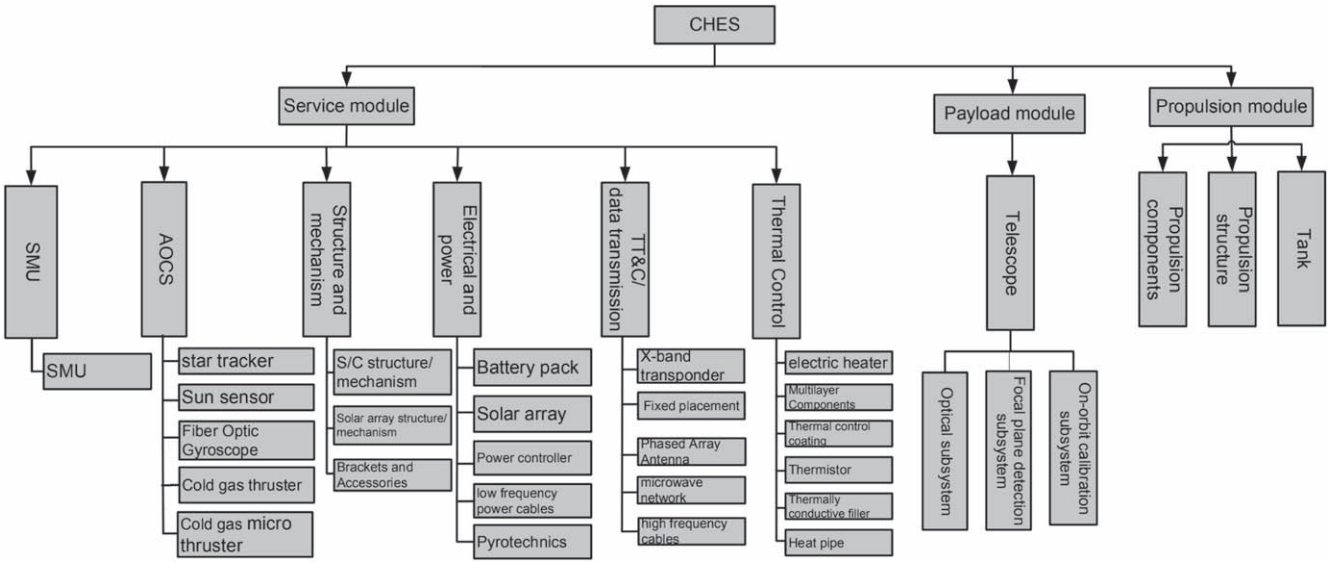

Figure 32. CHES composition.

Table 8
CHES Mass Allocation

No.	System	Mass kg^{-1}
1	Payload	765
2	Structure and mechanism	348
3	Thermal control	30
4	Electrical and power	61
5	AOCS	267
6	SMU	25
7	TT&C	32
8	Data transmission	30
9	S/C dry mass	1558
10	Propulsion module propellant	840
11	Service module propellant	150
12	Margin	382
	Total	2930

Table 9
CHES Power Allocation

No.	System	Orbit Entry Phase Power	Mission Phase Constant Power /W	Peak Power/W
1	Payload	0	650	700
2	Thermal control (Propulsion module)	100	0	200
3	Thermal control (except propulsion module)	30	50	80
4	Energy	25	25	25
5	AOCS	60	120	820
6	SMU	45	68	68
7	TT&C	35	25	95
8	Data transmission	0	195	195
9	Margin	30	110	210
	Total	325	1243	2393 (1493)

Considering that the current TRL is five, there are still further measures that can improve the technology maturity: Combining the operating mode of the CHES payload and the characteristics of the output stellar position information, we can develop the FGS simulator to form a full-link attitude control semi-physical closed-loop simulation system to verify the attitude control index.

5.3.4.2 High-precision thermal control. The telescope's high-precision thermal control technology is the key technology of the whole satellite. In terms of technology inheritance: (1) multi-stage thermal control technology, based on the Taiji-1 satellite launched in September 2019, adopts three-stage temperature control technology, with an on-orbit measured

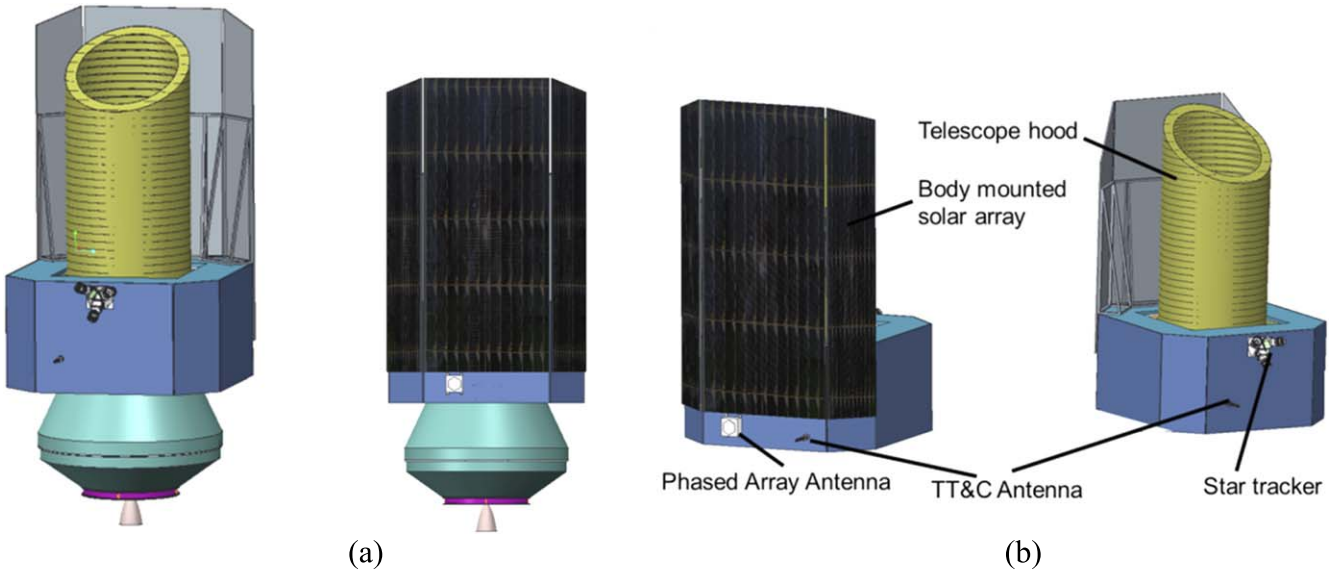

Figure 33. (a) Satellite retraction status; (b) Extra-satellite equipment layout.

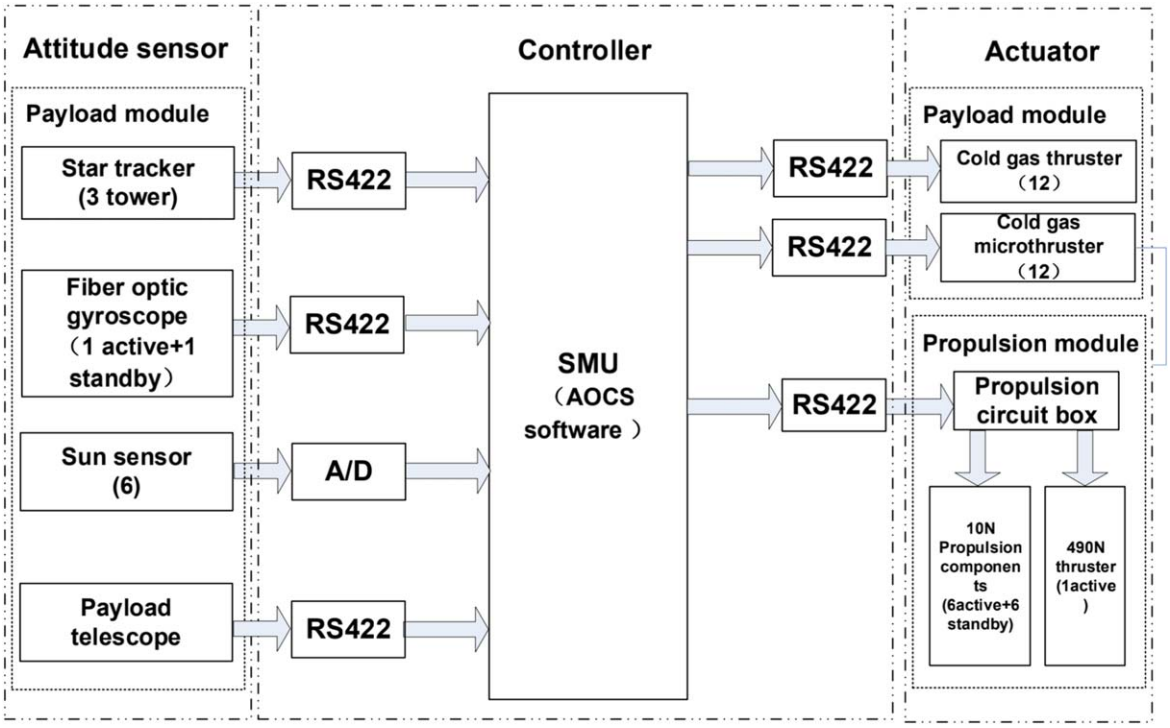

Figure 34. AOCS composition.

core area temperature control accuracy of 6 mK. (2) Ultra-high precision thermal control technology: based on the gravitational wave detection project. a. High-resolution low-noise temperature measurement: completed the prototype development and test verification of the thermometer, with a temperature resolution of 0.01 mK; b. High precision high thermal stability temperature control: the principle prototype design was completed; c. High thermal stability active heating temperature control algorithm research: the actual physical model and temperature control algorithm coupling under the mK level active temperature control was realized. The ultra-high-precision thermal control technology has completed the key technology research and review, part of which has developed a stand-alone machine, not yet in orbit flight

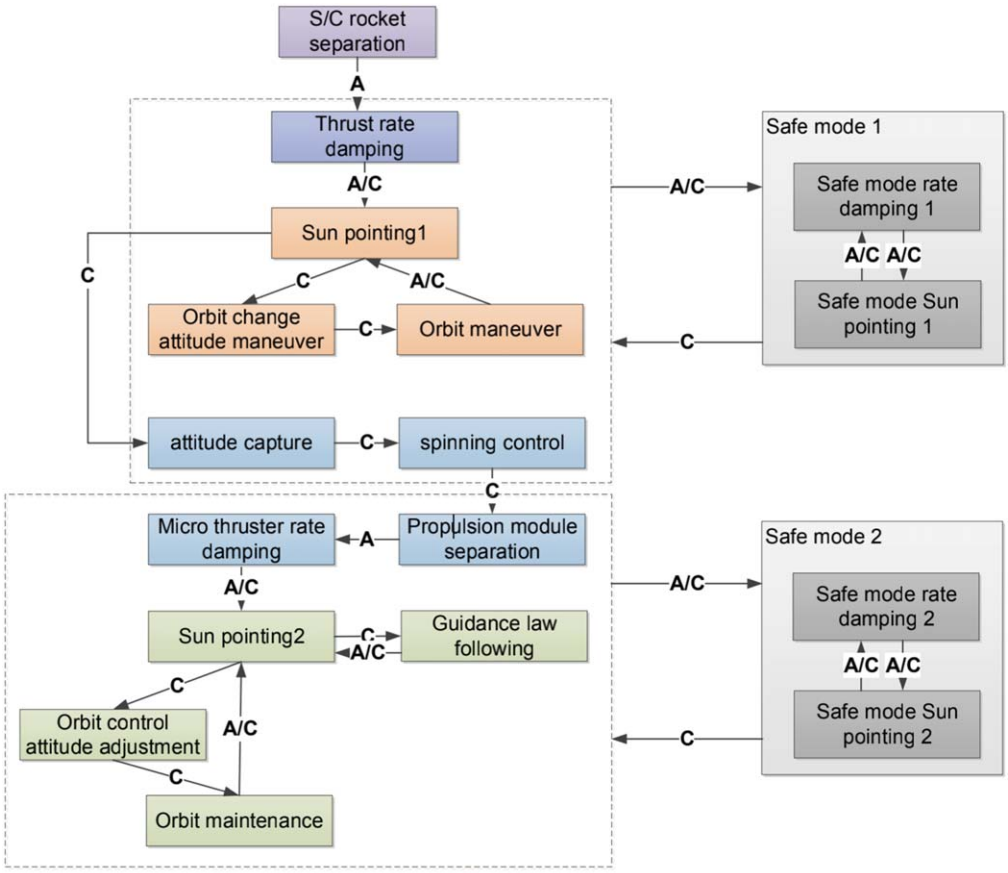

Figure 35. AOCS working modes.

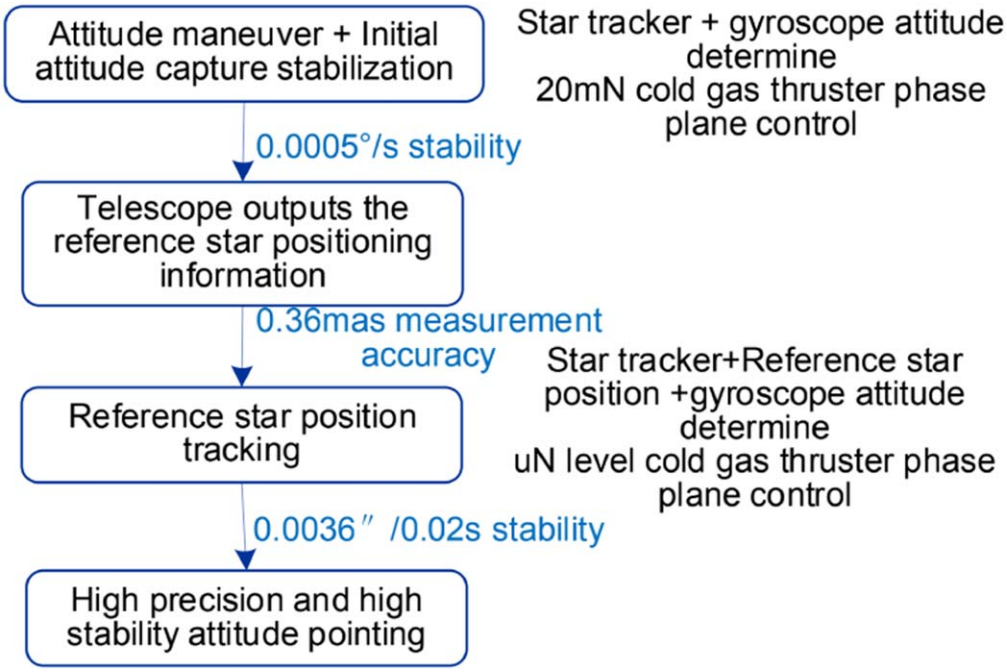

Figure 36. High-precision and high-stability attitude control process.

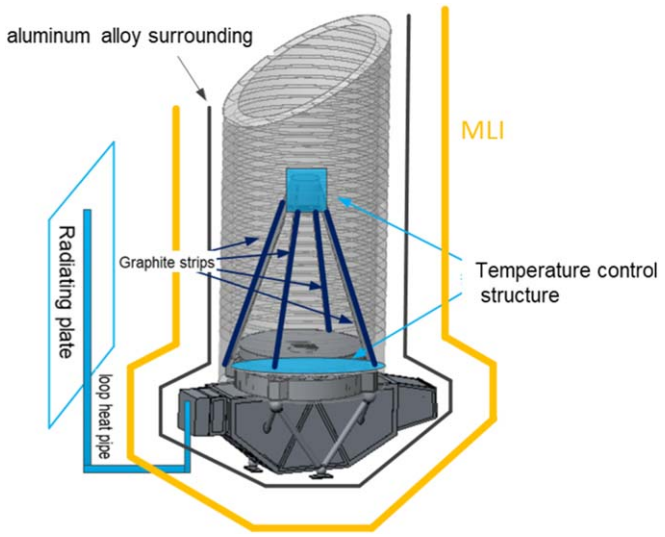

Figure 37. Telescope's thermal control design diagram.

verification, the relevant technology is to be used in the follow-up detection mission of the Taiji project.

Comprehensive consideration of the current stage of TRL reaches five, to further improve the TRL measures: on the basis of simulation analysis, put into production load thermal control for vacuum thermal tests to verify the thermal control scheme.

In summary, the CHES mission will discover Earth-like planets in the habitable zone around nearby solar-type stars via microarcsecond accuracy relative astrometry. CHES will offer the first direct measurements of true masses and three-dimensional orbits of Earth Twins and super-Earths orbiting our neighboring stars based on ultra-high-precision astrometry from space. In addition, CHES will further conduct a comprehensive survey and extensively characterize the nearby planetary systems. As to additional scientific benefits, CHES will partly offer informative clues to cosmology, dark matter and compact objects. This will definitely enhance our understanding of the formation of diverse nearby planetary systems and the emergence of other worlds for nearby solar-type stars, and finally provide guidance about the evolution of our solar system.

Acknowledgments

We thank the referee for constructive comments and suggestions that improved the manuscript. This work is financially supported by the Strategic Priority Research Program on Space Science of the Chinese Academy of Sciences (Grant No. XDA 15020800), the National Natural Science Foundation of China (Grant Nos. 12033010, 41604152 and U1938111), Foundation of Minor Planets of the Purple Mountain Observatory and Youth Innovation Promotion Association CAS (Grant No. 2018178).

References

Anglada-Escudé, G., Amado, P. J., Barnes, J., et al. 2016, Natur, 536, 437
Batalha, N. M., Rowe, J. F., Bryson, S. T., et al. 2013, ApJS, 204, 24
Berger, T. A., Huber, D., Gaidos, E., & van Saders, J. L. 2018, ApJ, 866, 99
Borucki, W. J., Agol, E., Fressin, F., et al. 2013, Sci, 340, 587
Borucki, W. J., Koch, D., Basri, G., et al. 2010, Sci, 327, 977
Borucki, W. J., Koch, D. G., Basri, G., et al. 2011, ApJ, 736, 19
Brandl, B. R., Lenzen, R., Pantin, E., et al. 2012, Proc. SPIE, 8446, 84461M
Broeg, C., Fortier, A., Ehrenreich, D., et al. 2013, EPJConf, 47, 03005
Brown, R. A. 2009, ApJ, 699, 711
Catanzarite, J., Tanner, A., & Shao, M. 2005, AAS Meeting Abstracts, 206, 14.04
Chen, D. 2014, JInst, 9, C04040
Chiang, E., & Laughlin, G. 2013, MNRAS, 431, 3444
Clementini, G., Ripepi, V., Leccia, S., et al. 2016, A&A, 595, A133
Des Marais, D. J., Harwit, M. O., Jucks, K. W., et al. 2002, Astrobiology, 2, 153
Fitzgerald, M., Bailey, V., Baranec, C., et al. 2019, BAAS, 51, 251
Fulton, B. J., Petigura, E. A., Howard, A. W., et al. 2017, AJ, 154, 109
Gao, M., Zhao, G., & Gu, Y. 2015, Bulletin of Chinese Academy of Sciences, 30, 721
Gaudi, B. S., Seager, S., Mennesson, B., et al. 2020, arXiv:2001.06683
Gillon, M., Triaud, A. H. M. J., Demory, B.-O., et al. 2017, Natur, 542, 456
Green, J., Schechter, P., Baltay, C., et al. 2012, arXiv:1208.4012
Günther, M. N., Pozuelos, F. J., Dittmann, J. A., et al. 2019, NatAs, 3, 1099
Hawker, G. A., & Parry, I. R. 2019, MNRAS, 484, 4855
Huang, C. X., Burt, J., Vanderburg, A., et al. 2018, ApJL, 868, L39
Jin, S., Ding, X., Wang, S., Dong, Y., & Ji, J. 2022, MNRAS, 509, 4608
Jin, S., & Mordasini, C. 2018, ApJ, 853, 163
Kaltenegger, L. 2017, ARA&A, 55, 433
Kasper, M., Cerpa Urra, N., Pathak, P., et al. 2021, Msngr, 182, 38
Koch, D. G., Borucki, W., Webster, L., et al. 1998, Proc. SPIE, 3356, 599
Kopparapu, R. K., Ramirez, R., Kasting, J. F., et al. 2013, ApJ, 765, 131
Krissansen-Totton, J., Garland, R., Irwin, P., & Catling, D. C. 2018, AJ, 156, 114
Krödel, M., Wächter, D., Stahr, F., & Soose, C. P. 2014, Proc. SPIE, 9151, 91510K
Lindegren, L., & Perryman, M. A. C. 1996, A&AS, 116, 579
Liu, B., & Ji, J. 2020, RAA, 20, 164
Luger, R., Sestovic, M., Kruse, E., et al. 2017, NatAs, 1, 0129
Macintosh, B., Troy, M., Doyon, R., et al. 2006, Proc. SPIE, 6272, 62720N
Madhusudhan, N. 2019, ARA&A, 57, 617
Malbet, F., Goullioud, R., Lagage, P.-O., et al. 2012, Proc. SPIE, 8442, 84420J
Marco-Hernández, R. 2020, Instruments, 4, 36
Mayor, M., & Queloz, D. 1995, Natur, 378, 355
Mordasini, C., Alibert, Y., Benz, W., & Naef, D. 2009, A&A, 501, 1161
Nemati, B., Shao, M., Gonzalez, G., et al. 2020, Proc. SPIE, 11443, 114430O
Owen, J. E., & Wu, Y. 2017, ApJ, 847, 29
Ragazzoni, R., Magrin, D., Rauer, H., et al. 2016, Proc. SPIE, 9904, 990428
Raymond, S. N., Mandell, A. M., & Sigurdsson, S. 2006, Sci, 313, 1413
Ricker, G. R., Winn, J. N., Vanderspek, R., et al. 2015, JATIS, 1, 014003
Shao, M., & Nemati, B. 2009, PASP, 121, 41
Skidmore, W., et al. 2015, RAA, 15, 1945
Snellen, I., de Kok, R., Birkby, J. L., et al. 2015, A&A, 576, A59
Tan, D.-J., Liu, J.-C., Zhu, Z., & Liu, N. 2022, RAA, 22, 025008
The LUVOIR Team 2019, arXiv:1912.06219
The Theia Collaboration, Boehm, C., Krone-Martins, A., et al. 2017, arXiv:1707.01348
Tinetti, G., Drossart, P., Eccleston, P., et al. 2016, Proc. SPIE, 9904, 99041X
Traub, W. A. 2016, arXiv:1605.02255
Tsiaras, A., Waldmann, I. P., Tinetti, G., Tennyson, J., & Yurchenko, S. N. 2019, NatAs, 3, 1086
Verlaan, A. L., Hogenhuis, H., Pijnenburg, J., et al. 2012, Proc. SPIE, 8450, 845003
Wang, J., Mawet, D., Ruane, G., Hu, R., & Benneke, B. 2017, AJ, 153, 183
Westerhoff, T., Davis, M., Hartmann, P., Hull, T., & Jedamzik, R. 2014, Proc. SPIE, 9151, 91510R
Zhang, X. 2020, RAA, 20, 099
Zhu, W., & Dong, S. 2021, ARA&A, 59, 291